

# Slitless spectrophotometry with forward modelling: principles and application to atmospheric transmission measurement

J. Neveu<sup>1,2</sup>, V. Brémaud<sup>2</sup>, P. Antilogus<sup>1</sup>, F. Barret<sup>3</sup>, S. Bongard<sup>1</sup>, Y. Copin<sup>4</sup>, S. Dagoret-Campagne<sup>2</sup>, C. Juramy<sup>1</sup>, L. Le Guillou<sup>1</sup>, M. Moniez<sup>2</sup>, E. Sepulveda<sup>1</sup>, and The LSST Dark Energy Science Collaboration

<sup>1</sup> Sorbonne Université, CNRS, Université de Paris, LPNHE, 75252 Paris Cedex 05, France

<sup>2</sup> Université Paris-Saclay, CNRS, IJCLab, 91405, Orsay, France

<sup>3</sup> MODAL'X, UPL, Univ. Paris Nanterre, CNRS, F92000 Nanterre France

<sup>4</sup> Univ Lyon, Univ Claude Bernard Lyon 1, CNRS/IN2P3, IP2I Lyon, UMR 5822, F-69622, Villeurbanne, France

July 12, 2023

## ABSTRACT

**Context.** In the next decade, many optical surveys will aim to tackle the question of dark energy nature measuring its equation of state parameter at the permil level. This requires to trust the photometric calibration of the survey with a precision never reached so far, controlling many sources of systematic uncertainties. The measurement of the on-site atmospheric transmission for each exposure, or on average for each season or for the full survey, can help reaching the permil precision for magnitudes.

**Aims.** This work aims at proving the ability to use slitless spectroscopy for standard star spectrophotometry and its use to monitor on-site atmospheric transmission as needed for example by the Vera C. Rubin Observatory Legacy Survey of Space and Time supernova cosmology program. We fully deal with the case of a disperser in the filterwheel which is the configuration chosen in the Rubin Auxiliary Telescope.

**Methods.** The theoretical basis of the slitless spectrophotometry is at the heart of our forward model approach to extract spectroscopic information from slitless data. We developed a publicly available software called **Spectractor** (<https://github.com/LSSTDESC/Spectractor>) that implements each ingredient of the model and finally performs a fit of a spectrogram model directly on image data to get the spectrum.

**Results.** We show on simulations that our model allows to understand the structure of spectrophotometric exposures. We also demonstrate its use on real data, solving specific issues and illustrating how our procedure allows the improvement of the model describing the data. Finally we discuss how this approach can be used to directly extract atmospheric transmission parameters from data, and thus provide the base of on-site atmosphere monitoring. We show the efficiency of the procedure on simulations, and test it on the limited data set available.

**Key words.** Astronomical instrumentation, methods and techniques - Atmospheric effects - Instrumentation: spectrographs - Techniques: imaging spectroscopy - Cosmology: observations

## 1. Introduction

Cosmology measures and interprets the evolution of the whole universe. To probe its dynamic and understand the nature of dark energy, observers need to compute distances at different epochs, from the light they receive in telescopes. The evolution of cosmological distances with time tells how dark energy, dark matter and matter interacts and how they can be modelled.

Optical surveys use magnitude and colour comparisons to build a relative distance scale. For instance, type Ia supernovae (SNe Ia) revealed the presence of a dark energy component because they appeared fainter in the early universe than it was thought (Riess et al. 1998; Perlmutter et al. 1999; Betoule, M. et al. 2014; Scolnic et al. 2018). More precisely, because SNIa colours redshift with universe expansion, high redshift supernovae were fainter in red bands than what can be inferred from low redshift supernovae observed in blue bands. This case underlines that colours need to be accurately calibrated in an optical survey to display the universe dynamics (see e.g., Betoule et al. 2013). Every chromatic effect that alters the astral light

distorts our dynamic perception of the universe expansion, like the galactic dust, the instrumental response or the local atmospheric conditions.

In this paper we present a forward modelling method to analyse and extract data gathered with a dispersing element (grating or hologram) in the filter wheel of a telescope. We label our approach as *forward modelling* because we implement a numerical simulation of the data taking procedure including as much *a priori* knowledge as is available, and then estimate model parameters from likelihood maximisation. This method is fundamentally different from the traditional flux weighted sum orthogonally to the dispersion axis (Horne 1986; Robertson 1986) or algebraic method using multiple images (Ryan et al. 2018) as it relies on physical modelling to describe directly the footprint of the spectrum on the imaging sensor. Deconvolution techniques and PSF modelling have been explored for optical fibre spectrographs (Bolton & Schlegel 2010; Li et al. 2019) but in our forward model we aim at going further in building a physical model for the extraction of the spectra, and in particular the atmospheric transmission from spectra. Our approach

was inspired by the forward modelling developed in [Outini & Copin \(2020\)](#), and we applied it for punctual sources, with the ultimate goal to measure atmospheric transmission.

The scientific context of our work is the study of the atmospheric transmission variability via the repeated observation of stable (aka standard) stars. [Burke et al. \(2010\)](#) opens the path to control the optical survey photometry with dedicated measurements of atmospheric components, observing standard stars. Then [Burke et al. \(2017\)](#) reached a 5 permil (i.e., “per thousand”) relative photometric calibration between filters covering the full optical and the near-infrared (near-IR) range, accounting for linear temporal variations of the atmosphere transmission over the nights. Given the scale of the new SNe Ia surveys, the number of observed objects reaches a point where even such an exquisite calibration stands as the dominant source of systematics. Being able to accurately measure and estimate the chromatic variations of the atmospheric transmission that allow us to probe for systematic variations, either nightly, seasonal or directional, at the per thousand level thus becomes one of the challenges of modern SNe Ia cosmology.

While spectrophotometry at the required precision has been hinted at in [The Nearby Supernova Factory et al. \(2013\)](#); [Rubin et al. \(2022\)](#), it relies on the dedicated use of a specifically designed integral field spectrograph. Our current approach instead focusses on exploring the spectrophotometric possibilities offered by a much simpler design: we consider a slitless spectrograph, where a disperser (either a grating or a hologram) is inserted in the converging beam of a telescope in a regular filter wheel. This implementation is used in the Rubin Auxiliary Telescope (AuxTel) ([Ingraham et al. 2020](#)), as well as on the Star Direct Illumination Calibration Experiment (StarDICE) telescope, an experiment aiming at transferring to stars the unit of optical power (watt) defined at the National Institute of Standards and Technology (NIST) with a reference cryogenic radiometer, Primary Optical Watt Radiometer (POWR) ([Houston & Rice 2006](#); [Hazenberg 2019](#); [Betoule, Marc et al. 2023](#)).

This paper describes the preparatory work for those projects, presenting the analysis procedure developed and tested on a few nights of data gathered at the Cerro Tololo Inter-American Observatory (CTIO). It describes some implementation choices, and demonstrates how the forward modelling approach allows us to incrementally build a detailed understanding of the data that in the end can permit the direct extraction of the parameters used to describe the atmospheric transmission variability.

The first section of this paper describes the theory of slitless spectrophotometry, the basic implementation in `Spectractor` and the data and simulations sets to assess the quality of the algorithm. Section 3 details the different ingredients of the `Spectractor` software, the assumptions and the implementation choices. In particular we detail the regularised deconvolution technique at the heart of the process to get a prior for the forward model, and qualify the code on simulations. The application of `Spectractor` to extract spectra from on-sky CTIO data is described in section 4, while section 5 is focussed on the measurement of the atmospheric transmission. Discussions and summaries conclude the paper in section 6.

## 2. Forward modelling of a slitless spectrum

There are many different possible configurations to gather spectroscopic data without the use of a slit. The slitless spectrograph configuration that will be considered in this paper (a grating or hologram in a converging beam) can be implemented in different ways that could require special care in the forward-modelling analysis. For example, the field of view can be small and contain only one star, or it can be crowded, with many star spectrograms super-imposing on each other. There might be different detectors spanning the field of view, with responses that need to be mapped and gaps that need to be accounted for. We haven’t tried to solve abstractly all different situations. We therefore defer to further work all the technical issues that we didn’t encounter, and concentrate on the ones we did and solved.

Among those restrictions, we consider in the following only the case of point sources and won’t discuss, aside from a passing mention in the next section, the case of extended sources like galaxies or resolved planetary nebulae, nor the deblending of such extended sources with point sources.

### 2.1. Description and geometry of a slitless spectrograph

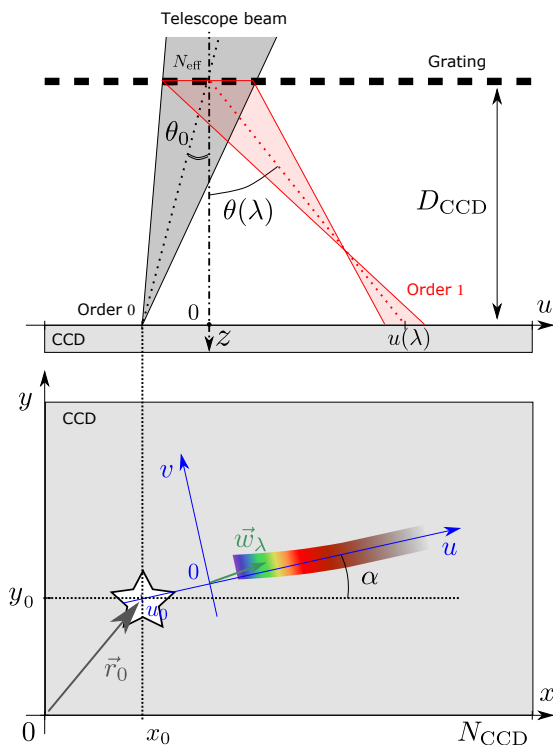


**Fig. 1.** Geometry of a simple slitless spectrograph in the plane orthogonal to the CCD (top) and parallel to the CCD (bottom). A convergent beam with incident angle  $\theta_0$  is focused on a CCD at position  $\mathbf{r}_0 = (x_0, y_0)$ , but also passed through a grating with  $N_{\text{eff}}$  grooves per millimetre at a distance  $D_{\text{CCD}}$  above the CCD. The beam is deflected at an angle  $\theta(\lambda)$  along the mean dispersion axis  $u$  which forms an angle  $\alpha$  with respect to the CCD  $x$  axis, but is focused somewhere above the sensor. Atmospheric refraction adds a supplementary dispersion along and transversally to the mean dispersion axis.

The slitless spectrograph we consider can be seen as a grating with  $N$  grooves per millimetre, placed in a telescope

beam at a distance  $D_{\text{CCD}}$  from a Charge-Coupled Device (CCD) sensor. In the following, the positions in the sensor plane are parametrised with the coordinates  $\mathbf{r} = (x, y)$  and the  $z$  axis points orthogonally toward the CCD. The disperser can be more or less complex, used in a convergent or in a parallel beam, and it can have a varying resolution, but in the end it will spread the source light in different diffraction orders superimposed on the CCD, with a sky background also diffracted. Depending on the choice of  $N$ , on the size  $N_{\text{CCD}}$  (in pixels) of the sensor and on  $D_{\text{CCD}}$ , different diffraction orders will end up to be recorded by the sensor.

The special case of the 0th order is worth mentioning: while its presence on the image is not mandatory, knowing its centroid position  $\mathbf{r}_0$  can ease significantly the setting of the zero of the wavelength calibration.

The positive and negative diffraction orders are placed on each side of the 0th order on a line forming an angle  $\alpha$  with the  $x$  axis. We parametrize the position along this dispersion axis with the coordinate  $u$  and transversally with the coordinate  $v$ . The zeroth order stands at coordinates  $(u_0, 0)$  in the  $(u, v)$  coordinate system. If the instrument wavelength coverage spans more than one octave in wavelength, the different diffraction orders superimpose on each other.

The total 2D CCD image formed by the cumulation of the collected light is called hereafter a *spectrogram*. All the notations are illustrated in Figure 1.

For a periodic grating placed inside a convergent beam instead of a parallel beam, this optical system response is astigmatic i.e., the image of a point source like a star is not point-like on the sensor. Usually, the image is elliptical, and the redder the wavelength the wider the ellipse (see e.g., Moniez et al. 2021). However, the centroid of these ellipses is still given by the classical grating formula (see e.g., Murty 1962; Hall 1966; Schroeder & Inc 2000) :

$$\sin \theta_p(\lambda) - \sin \theta_0 = p N_{\text{eff}} \lambda, \quad (1)$$

$$\tan \theta(\lambda) = \frac{u(\lambda)}{D_{\text{CCD}}}, \tan \theta_0 = \frac{u_0}{D_{\text{CCD}}}. \quad (2)$$

The angles are those of the projection in the plane perpendicular to the grating lines (see Figure 1);  $\theta_0$  is the angle of the projected telescope beam axis with respect to the normal to the grating surface,  $p$  is the diffraction order,  $\theta_p(\lambda)$  is the corresponding projected diffracted angle, and  $N_{\text{eff}}$  is the effective spatial frequency of grating lines at the position of the central ray<sup>1</sup> of the light beam (hereafter called chief ray).

The observer has the liberty to choose the focus of the telescope. One common choice is to set the focus using the order 0 but doing so the spectrogram can suffer from defocusing effects going toward redder wavelengths (for periodic gratings). To minimize the defocusing effect and increase the spectrograph resolution, it is possible to optimize the focus for a particular wavelength, but then it is more difficult to set the zero of the wavelength calibration with a defocused order 0 image. In the following we assume that the focus has been made on the 0th order, unless otherwise specified.

<sup>1</sup> For some dispersers this number of lines per millimetre can depend on the beam position on the grating.

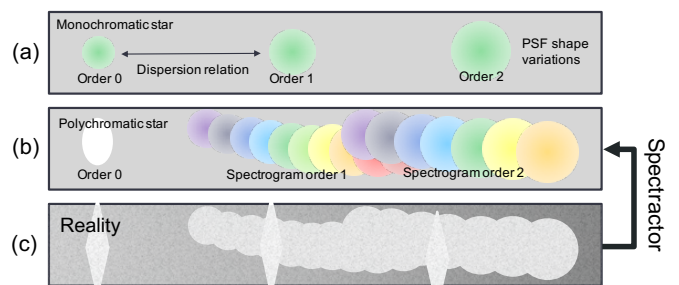


**Fig. 2.** General illustration of the spectrograph model and of the purpose of the spectrum extraction. (a) Illustration of the image formation for a monochromatic star observed through a slitless spectrograph. (b) Same for a polychromatic star. (c) Real acquired image: the detector is generally a black and white sensor, with noise, a structured and chromatic background, and field star 0th- and 1st-order spectrograms. The goal of **Spectrator** is to extract the color information from this image to get the star spectrum.

## 2.2. Theoretical model of a spectrogram

A theoretically perfect image of a light source can be modelled by its spatio-spectral flux density  $C(\mathbf{r}, \lambda)$ . For a point source, we can separate the spectral and spatial distributions as:

$$S_*(\mathbf{r}, \lambda) = S_*(\lambda) \times \delta(\mathbf{r} - \mathbf{r}_0) \quad (3)$$

with  $S_*(\lambda)$  the astrophysical object spectral energy density (SED) and  $\delta$  the Dirac distribution. The observed spectral and spatial distribution is then:

$$C_p(\mathbf{r}, \lambda) = T_{\text{inst},p}(\lambda) T_{\text{atm}}(\lambda | \mathbf{P}_a) S_*(\mathbf{r}, \lambda) \quad (4)$$

where  $T_{\text{atm}}(\lambda | \mathbf{P}_a)$  is the atmospheric transmission, depending on a set of atmospheric parameters  $\mathbf{P}_a$ ,  $T_{\text{inst},p}(\lambda)$  is the instrumental transmission (including the CCD quantum efficiency) for the diffraction order  $p$ .

In the case of a monochromatic point source we have  $C_0(\mathbf{r}, \lambda) = A \delta(\lambda - \lambda_0) \times \delta(\mathbf{r} - \mathbf{r}_0)$  with  $A$  the received source flux at  $\lambda_0$ . The Point Spread Function (PSF) describes the optical response of the telescope and of the atmospheric turbulence on a sensitive surface like a CCD (see Figure 2 (a)). It depends *a priori* on the wavelength  $\lambda$  and can be modelled by a function  $\phi_0(\mathbf{r}, \lambda)$  whose spatial integral is normalised to one. Therefore, by definition of the PSF, the image of a monochromatic point source centred on  $\mathbf{r}_0$  on the CCD can be described as a convolution product:

$$\begin{aligned} I_0(\mathbf{r}) &= \int d\lambda \iint d^2\mathbf{r}' C_0(\mathbf{r}', \lambda) \phi_0(\mathbf{r} - \mathbf{r}', \lambda) \\ &= A \phi_0(\mathbf{r} - \mathbf{r}_0, \lambda_0). \end{aligned} \quad (5)$$

With a slitless spectrograph, the mechanism is the same but the incoming light is dispersed in several diffraction orders  $p$ , and light from all diffraction orders of the sky background is superimposed. The position of the point source image depends on the wavelength and the order  $p$ . Also the PSF shape itself can depend on the order  $p$  and the wavelength  $\lambda$ . Here and everywhere else, the dispersed imaging PSF integrates both the seeing and the instrumental PSF. Let's introduce the dispersion relation  $\Delta_p(\lambda)$  as the 2D vectorial quantity that describes the position of the PSF

centroids  $\{x_{c,p}(\lambda) - x_0, y_{c,p}(\lambda) - y_0\}$  on the CCD with respect to the zeroth order position  $(x_0, y_0)$ , for a diffraction order  $p$  and a wavelength  $\lambda$ . This quantity can be computed by applying the classical grating formula 1. With a point-like monochromatic source, the image recorded on the CCD is modelled as:

$$\begin{aligned} I(\mathbf{r}) &= \sum_p \int d\lambda \iint d^2\mathbf{r}' C_p(\mathbf{r}', \lambda) \phi_p(\mathbf{r} - \mathbf{\Delta}_p(\lambda) - \mathbf{r}', \lambda) \\ &= \sum_p A_p \phi_p(\mathbf{r} - \mathbf{\Delta}_p(\lambda_0), \lambda_0), \end{aligned} \quad (6)$$

with  $\mathbf{\Delta}_0(\lambda_0) = \mathbf{r}_0$  and  $A_p$  the flux density at wavelength  $\lambda_0$  for the order  $p$ . On the image, one expects a series of spots, one per order  $p$ , of different intensities, with different sizes, but containing the same spectral information  $S_*(\lambda_0)$  about the source.

The observed sources are naturally polychromatic. For point-like sources, the theoretical description above holds at each wavelength and the image can be described as:

$$I(\mathbf{r}) = \sum_p \int d\lambda S_p(\lambda) \phi_p(\mathbf{r} - \mathbf{\Delta}_p(\lambda), \lambda), \quad (7)$$

with

$$\mathbf{\Delta}_p(\lambda) = \{x_{c,p}(\lambda) - x_0, y_{c,p}(\lambda) - y_0\}, \quad (8)$$

$$S_p(\lambda) = T_{\text{inst},p}(\lambda) T_{\text{atm}}(\lambda | \mathbf{P}_a) S_*(\lambda). \quad (9)$$

Therefore, the spectrogram of a polychromatic source can be viewed of as a stack of monochromatic images with different centroids, or as a dispersed image with a very chromatic PSF (see Figure 2 (b)). This description of the image and of the spectrogram formation is the base of our forward model of slitless spectrograph data.

To obtain the  $S_p(\lambda)$  spectra, a process to un-stack the monochromatic images spread over the image by the disperser is needed (Figure 2 (c)). This in turn requires that such ingredients as the PSF  $\phi_p(\mathbf{r}, \lambda)$  and the dispersion relation  $\mathbf{\Delta}_p(\lambda)$  are sufficiently well known, either *a priori*, either thanks to specific data analysis, or directly fitted on data. The hardest point is usually the determination of the PSF kernel as a function of wavelength. Indeed, as illustrated in Figures 1 and 2, in the general case the PSF is blurred and defocused. Using a simple Moffat profile to model the PSF is suitable as long as the defocus is small; we did this approximation along this paper and we leave the general defocus case for future work. Nevertheless, we studied and discussed two cases: the use of a standard grating and the use of an holographic disperser that limits the defocus.

In this paper we describe our implementation of such a process in the form of the `python3 Spectractor` code Neveu et al. (2021) (see Section 3). We also show how we tested it on simulations and data, as well as showing how it could be used in order to ingest lacking modelling information from specific data analysis.

### 2.3. Spectractor

We call `Spectractor`<sup>2,3</sup> the computer suite we wrote to analyse the future AuxTel images, as well as the images

<sup>2</sup> <https://github.com/LSSTDESC/Spectractor>

<sup>3</sup> <https://spectractor.readthedocs.io>

obtained on the Cerro Tololo Inter-American Observatory (CTIO) 0.9 m telescope. It was trained on CTIO data but with the purpose to be easily configurable for slitless spectrophotometry with other telescopes. The main steps, inputs and outputs of the extraction part are illustrated in Figure 3 and will be described in details in Section 3. To help the reading of the following, here is a summary of the `Spectractor` main steps:

**Order 0 centroid:** The main inputs of `Spectractor` are a pre-processed image (overscan subtracted, debiased, spatial flat fielded) obtained with a slitless spectrograph, and a configuration file setting the main geometrical and spectrographic properties of the instrument ( $D_{\text{CCD}}$ ,  $N$ , telescope diameter, pixel size, the PSF model etc.) At the time of writing this paper, the PSF models implemented are either a Gaussian profile, a Moffat profile or a Moffat minus a Gaussian profile. Further more detailed PSF models are planned to describe more accurately the AuxTel data as it is analysed. We are in the situation where the centroid of the zeroth order is contained in the image. We thus implemented a searching procedure to inform us on the origin of the location of the spectrum and set the zero of the wavelength scale.

**Rotation:** Considering the geometry of the spectrograph and the dispersion properties of the grating, the spectrogram is cropped from the image and de-rotated to have the dispersion axis along the horizontal axis of the cropped image. Note that the rotation angle is fitted later in the full model without explicitly rotating the image.

**Geometric wavelength calibration:** On that image, a first fit of a 1D sliced PSF model transverse to the dispersion axis is performed, with PSF shape parameters represented by a polynomial function<sup>4</sup> as a function of the distance to the order 0.

**PSF deconvolution:** The procedure is continued by a deconvolution that uses a 2D PSF model and the 1D result as a prior to regularize it.

**Wavelength calibration:** A first wavelength calibration is performed using the detection of the principal absorption or emission lines in the extracted spectrum (astrophysical or telluric lines).

**Flux calibration:** spectrum flux in ADU is converted into  $\text{erg/s/cm}^2/\text{nm}$  units using the telescope collecting area, CCD gain and exposure time.

**Full forward model:** Finally, given all these prior ingredients, a full forward model is initiated on the preprocessed<sup>5</sup> but not rotated exposure using a 2D PSF model, and a

<sup>4</sup> A polynomial function of the fourth order is sufficient to absorb the main chromatic variations of the PSF shape.

<sup>5</sup> For future developments, one could model directly the unpre-processed exposure, for instance introducing the chromatic flat fields directly in the forward model.

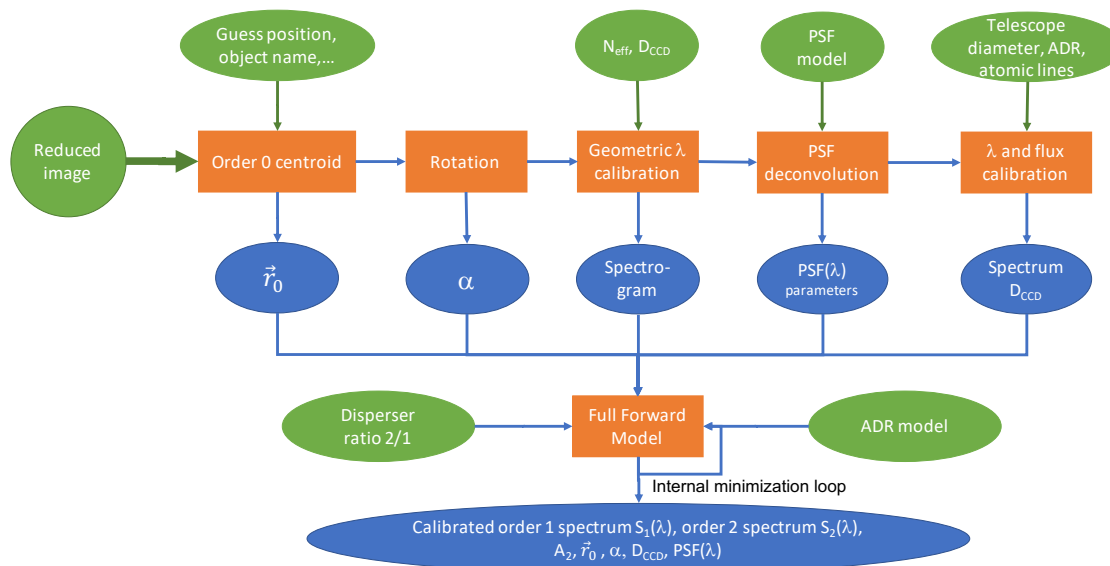


**Fig. 3.** Overview of the **Spectractor** pipeline. Green ellipses represent external inputs needed for the spectrum extraction, and blue ellipses stands for the **Spectractor** products. The bottom stage represents the full forward modelling method applied to extract the spectrum from the raw spectrogram.

model for the Atmospheric Differential Refraction (ADR)<sup>6</sup>. The PSF shape parameters as well as the wavelength calibration are refitted in the process. The main output is a calibrated spectrum in wavelength and amplitude, but **Spectractor** returns also a host of useful fitted parameters like the PSF shape chromaticity or the  $D_{\text{CCD}}$  distance, to perform extraction quality analysis and in the end to improve the forward modelling or its initialisation.

Note that all the steps but the last are implemented in order to provide the required ingredients to the full forward models, and are thus completely contingent to the availability of understanding of the instrument. This will again be addressed later on when we discuss how to obtain the optical transmission of the instrument.

## 2.4. Data examples

While we use the natural ability of the forward model implementation to easily provide simulations to validate the code, we also present the use of **Spectractor** on real data.

### 2.4.1. CTIO data

In order to test the slitless spectroscopy approach, in particular using a holographic disperser, we benefited of a run of 17 nights in May-June 2017 at the Cerro Tololo Inter-American Observatory (CTIO) 0.9 m Cassegrain telescope ( $f/13.7$ , scale at focal plane  $60 \mu\text{m}/''$ ). This telescope is equipped with a cooled Tek2K CCD device of  $2048 \times 2046$  pixels, read by four amplifiers<sup>7</sup>. Two filter wheels are installed. The first one in the light path was used to insert broad band filters, while the second one hold different dispersers.

While many gratings were tried, in this paper we focused on two of them: a Thorlabs blazed grating (300 lines/mm)

ref. GT50-03 and an amplitude holographic optical element (around 350 lines/mm) especially designed for this telescope. This hologram is fully described and analysed thanks to the CTIO data in Moniez et al. (2021). Its main advantage is that the defocusing described in Figure 1 is very limited, which allowed us to model its chromatic PSF with simpler mathematical models.

By using those dispersers in the upstream filter wheel, we readily transformed the CTIO 0.9 telescope into a spectrophotometric instrument with a resolution of about 150 – 200 (Moniez et al. 2021).

Figure 4 shows an example of the data obtained: The dispersion axes are nearly horizontal along the  $x$  axis of the CCD, and for optimal focusing of the amplitude hologram the target star was placed around pixel coordinates (750, 700). The spectrum covers two amplifiers. Field stars are present and the sky background is also dispersed (brighter in the middle).

Dome flats were taken with different filters, and we used a red one to flatten our exposures ( $\lambda > 715 \text{ nm}$ ). Combined bias were taken at the beginning of each night, for bias subtraction. We made sure that the meta data contains informations about the CCD properties and from the on-site meteorological station.

We mainly analysed the performances of the holographic element we brought during this run. Fortunately, we had one very good night on 2017 May 30th with very stable conditions in terms of temperature and seeing, which we can exploit to estimate atmospheric transmission. During that night we essentially monitored the CALSPEC<sup>8</sup> (Bohlin et al. 2014; Bohlin et al. 2020) star HD111980 with an amplitude hologram. The main characteristics of those data are summarised in Table 1.

<sup>6</sup> ADR is also called Differential Chromatic Refraction (DCR).

<sup>7</sup> <https://noirlab.edu/science/programs/ctio/instruments/Tek2K>

<sup>8</sup> <https://www.stsci.edu/hst/instrumentation/reference-data-for-calibration-and-tools/astronomical-catalogs/calspec>

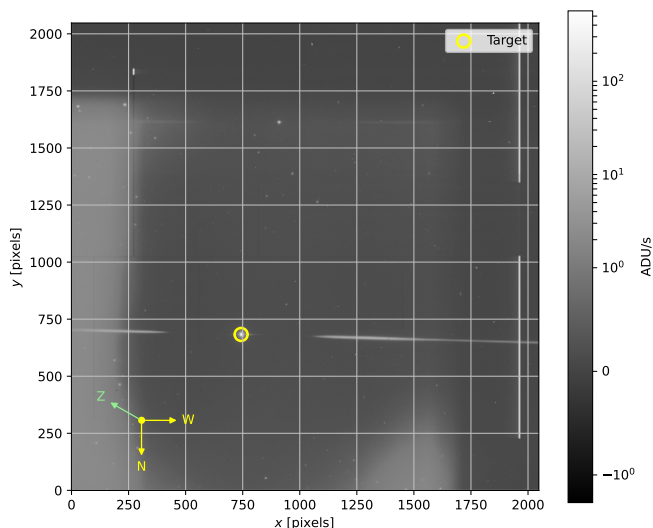


**Fig. 4.** Processed exposure of CALSPEC star HD111980 observed at CTIO with an amplitude hologram grating of 350 lines/mm on 2017, May 30th. The grey scale gives the exposure intensity in ADU/s. A yellow circle indicates HD111980 zeroth order position.

**Table 1.** Principal characteristics of the exposure used as an example in section 3.

Properties	Values
Observatory	CTIO 0.9 m
Disperser	Amplitude hologram $\approx$ 350 lines/mm
Dispersion axis angle $\alpha$	$\approx -1.6^\circ$
$D_{\text{CCD}}$	$\approx 56$ mm
Pixel size	24 $\mu\text{m}$
Pixel spectral scale	$\approx 1$ nm
Pixel angular scale	0''401
Target	CALSPEC HD111980
Exposure	120 s
Background level	$\approx 25$ ADU
Seeing	0''65
Airmass	1.13
Outside pressure	784 hPa
Outside temperature	8.6 $^\circ\text{C}$

#### 2.4.2. Simulations

To test **Spectractor** pipeline, we use the full forward model for CTIO spectrograms (see section 3.8) to simulate observations of CALSPEC stars (in particular HD111980).

The simulation used in Section 3 shares the same known characteristics as the real data image presented in Table 1, but with variations concerning unknown parameters like the PSF model, the amount of second order diffraction contamination and the atmospheric parameters.

For simulations, a 2D Moffat circular PSF kernel  $\phi(x, y, \lambda)$  is chosen. To model the widening of the PSF due to defocusing or chromatic seeing effects, shape parameters  $\gamma$  and  $\alpha$  evolves with wavelength as a  $n_{\text{PSF}}$  order polyno-

mial function:

$$\phi(x, y | \mathbf{r}_c, \mathbf{P}) = A \left[ 1 + \left( \frac{x - x_c}{\gamma(z(x))} \right)^2 + \left( \frac{y - y_c}{\gamma(z(x))} \right)^2 \right]^{-\alpha(z(x))} \quad (10)$$

$$A = \frac{\alpha - 1}{\pi \gamma^2} \quad \text{with } \alpha > 1, \quad (11)$$

$$\gamma(z) = \sum_{i=0}^{n_{\text{PSF}}} \gamma_i L_i(z), \quad \alpha(z) = \sum_{i=0}^{n_{\text{PSF}}} \alpha_i L_i(z). \quad (12)$$

The integral of this PSF kernel is exactly  $A$ , and its centre is at  $\mathbf{r}_c = (x_c, y_c)$ . The PSF shape parameters  $(\gamma(x), \alpha(x))$  are themselves sets of polynomial coefficients  $\gamma_i$  and  $\alpha_i$  respectively. The  $L_i(x)$  functions are the order  $i$  Legendre polynomials. Let's call  $x_{\text{min}}$  and  $x_{\text{max}}$  the left and right pixel positions of the spectrogram edges on the  $x$  axis. The parameter  $z \in [-1, 1]$  is rescaled proportionally on the desired pixel range  $[x_{\text{min}}, x_{\text{max}}]$ , set to encompass roughly the wavelength range [350 nm, 1100 nm] with the formula

$$z(x) = \frac{x - (x_{\text{max}} + x_{\text{min}})/2}{(x_{\text{max}} - x_{\text{min}})/2}. \quad (13)$$

Parametrisation with Legendre polynomials has the advantage to give an equal weight to all polynomial coefficients during  $\chi^2$  minimisation, whatever the degree of the polynomial functions. The chosen  $n_{\text{PSF}}$ ,  $\gamma_i$  and  $\alpha_i$  values are quoted for each simulation. Simulation suite is fully available in the **Spectractor** code.

### 3. Forward model extraction of a spectrum

In this section we follow and describe in detail the steps of the **Spectractor** pipeline in order to get the first order spectrum  $S_1(\lambda)$  of a point source, calibrated in flux and wavelength. Those steps cover the first line of orange boxes of figure 3, and leave to a later discussion the full forward model. The process starts from a preprocessed image containing the 2D image formed by a star observed through a slitless spectrograph that we call a spectrogram.

#### 3.1. Uncertainty evaluation

Once the exposure is pre-processed, if not given we must start to build the uncertainty map of the exposure. The uncertainties on the pixel values are estimated using the CCD gain  $G_{\text{CCD}}(x, y)$  (in electrons/ADU) and its read-out noise  $\sigma_{\text{ro}}$  (in electrons). The exposure unit is considered to be in ADU at that point. The uncertainty  $\sigma(x, y)$  on the pixel value  $I(x, y)$  is then:

$$\sigma(x, y) = \frac{1}{G_{\text{CCD}}(x, y)} \sqrt{\sigma_{\text{ro}}^2 + G_{\text{CCD}}(x, y) I(x, y)} \quad (14)$$

as we assume that the number of photoelectrons in each pixel follows a Poisson distribution. The uncertainty map can be inverted to get a weight map, on which we can superimpose a mask to remove bad pixels. Assuming no correlations between pixels, we then assemble a weight matrix  $\mathbf{W}$  as a diagonal matrix of the inverted pixel variances.

The computed noise variance uses the pixel value itself, which incorporates the noise fluctuation. Using weights incorporating the fluctuations is prone to introduce a bias

on the recovered quantities because in the case of positive fluctuation, the weight is increased while in the case of negative fluctuation the weight is decreased. The bias is smaller with high signal-to-noise spectrograms. For this reason, in simulations and data we will only consider the high signal-to-noise case and will avoid the bias due to this uncertainty evaluation (even at the spectrum edges where flux is low). The low signal-to-noise case is postponed for future developments.

### 3.2. Zeroth order centroid

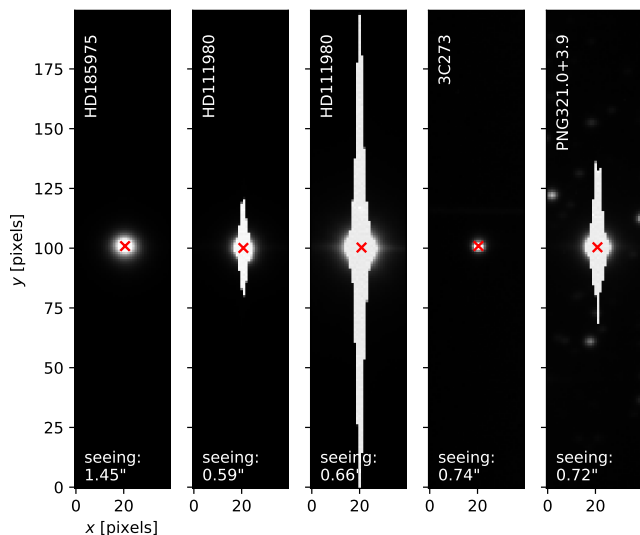


**Fig. 5.** Order 0 images from different celestial objects, observed in different seeing conditions with several dispersers. The red cross is the fitted centroid using the `Spectractor` method from section 3.2. All images have saturated pixels.

Since the zeroth order is included in the observed images, we use its centroid to set the zero of the wavelength scale. Therefore, an error in the determination of the zeroth order centroid  $(x_0, y_0)$  results in a systematic shift of the wavelength calibration.

A subset of different situations encountered in the CTIO data is presented in Figure 5. To get a high signal-to-noise in the spectrogram, the exposure time is set at such a value that the zeroth order is saturated, causing bleeding spikes. If the exposure comes with a World Coordinate System (WCS), then one can get the precise position of the star on the CCD. However, in most images we get from CTIO, the WCS associated with the images is wrong because of an imprecise mount calibration.

While not directly part of the extraction procedure, we present the algorithm we implemented to find the zeroth order centroid in such difficult cases as an useful example of how to improve the starting point from preliminary analysis of the data.

First, the image is cropped around the supposed position of the zeroth order image, as close as needed so that the targeted star is the brightest object. Then the cropped image is projected onto the  $x$  and  $y$  axis: the maximum of the two projections sets a new approximation of the order 0 position. From there, saturated pixels are detected and

a null weight is affected to them. A 2D second order polynomial background with a  $3\sigma$  outlier removal is fitted and subtracted from the cropped image. At last, a 2D circular Moffat profile is fitted on the weighted pixels: only the crown of non-saturated pixels counts and locks the fit. This last step is then repeated a second time on a new cropped image of width and height divided by two, centred in the last fitted centroid. This step is illustrated Figure 6. We tested this process on many images, most of them pathological, and visually confirmed that the accuracy of this algorithm is finer than the pixel size on CTIO images.

An other issue we had to cope with is that when adding a disperser on the telescope beam path, the WCS associated with the image can be shifted or distorted. In the case of crowded field, faint objects or very pathological order 0, we developed a method to estimate the WCS using the field stars, the library `astrometry.net`<sup>9</sup> (Lang et al. 2010) and the Gaia DR2 catalogue. The process is described in appendix A, but not used by default to deal with the CALSPEC stars we observed. However, when comparing the centroids obtained with both methods, their difference has a scatter of  $0''.15$  (around one half of a pixel) on CTIO data which confirms that both methods are accurate at least at the  $0''.15$  level (Figure 7).

This accuracy is converted into a prior on the order 0 shift  $\delta u_0$  used during the wavelength calibration process to account for a mistake in the order 0 centroid evaluation.

### 3.3. Rotation

Unless special care has been taken to that end when mounting the disperser in the filter wheel, the spectrogram image can be tilted (possibly intentionally) with respect to the  $x$  axis, with an angle which can be poorly known depending on the mounting of the disperser into the telescope beam.

This dispersion direction can be either known *a priori*, or fitted in the full forward model step. Since we are in the later case, we need a supplementary step to estimate a good starting point for this angle.

In addition, in the following we found it extremely useful to have the spectrogram to be roughly aligned with the  $x$  axis of the exposure, with the wavelength increasing with  $x$ . To that end exposure must be flipped and rotated accordingly before continuing the process of extracting more information useful both to diagnose the data quality, and to refine the starting point of the full forward model.

The spectrogram of sources sufficiently continuous in wavelength, like the thermal emission component of stars for example, display filament shapes on the 2D image that can be detected using an Hessian analysis inspired by the one developed in Ade et al. (2016). The advantage of this technique is that it comes with an analytical expression of the angle of the detected shape with respect to the horizontal or vertical axis of the CCD grid.

The Hessian matrix  $H(x, y)$  of the image is computed for each pixel value  $I(x, y)$  as:

$$H(x, y) = \begin{pmatrix} H_{xx} & H_{xy} \\ H_{xy} & H_{yy} \end{pmatrix} = \begin{pmatrix} \frac{\partial^2 I}{\partial x^2} & \frac{\partial^2 I}{\partial x \partial y} \\ \frac{\partial^2 I}{\partial x \partial y} & \frac{\partial^2 I}{\partial y^2} \end{pmatrix}. \quad (15)$$

<sup>9</sup> <http://astrometry.net/doc/readme.html>

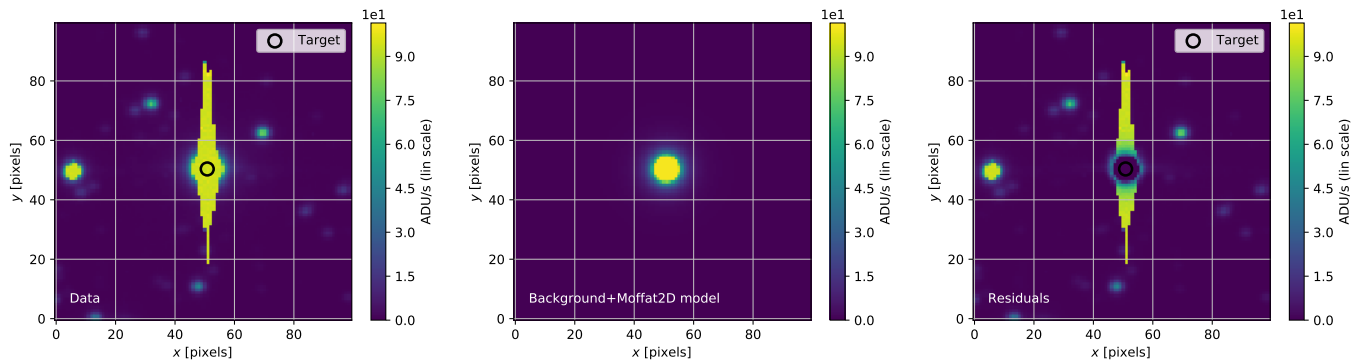


**Fig. 6.** Illustration of the fitting process to find the order 0 centroid, on planetary nebula PNG321.0+3.9. *Left:* order 0 data image of the target. *Middle:* best-fitting 2D circular Moffat model. *Right:* residuals.

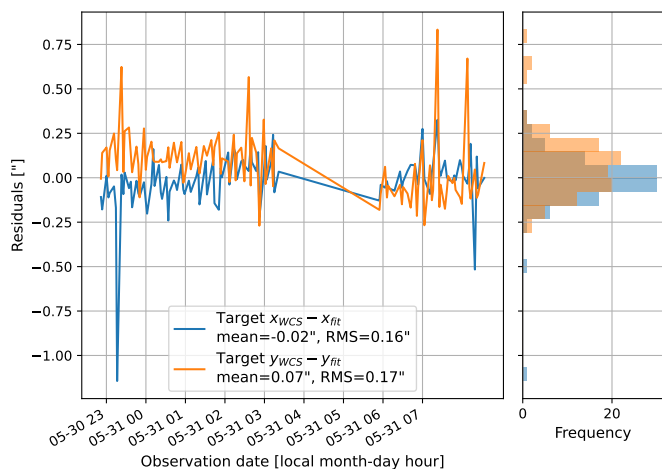


**Fig. 7.** Difference between the fitted centroids of the target stars and the centroid recovered using the WCS estimate locked on the Gaia catalogue (blue and orange lines) on the  $x$  and  $y$  axis at CTIO during the night of 2017, May 30th, as a function of the exposure date. The histogram of the differences is presented on the right.

The two eigenvalues of the Hessian matrix  $H$  are calculated as

$$\lambda_{\pm}(x, y) = \frac{1}{2} (H_{xx} + H_{yy} \pm h) \quad (16)$$

with  $h = \sqrt{(H_{xx} - H_{yy})^2 + 4H_{xy}^2}$ . The eigenvalue  $\lambda_-$  is associated with the eigenvector directed along the spectrum dispersion axis while  $\lambda_+$  corresponds to the eigenvector with the largest change in intensity value i.e., transverse to the dispersion axis. The orientation angle of these eigenvectors with respect to the  $x$  axis can be analytically computed. For instance for  $\lambda_-$  we have:

$$\begin{aligned} \alpha(x, y) &= \arctan\left(\frac{H_{yy} - H_{xx} - h}{2H_{xy}}\right) \\ &= \frac{1}{2} \arctan\left(\frac{2H_{xy}}{H_{xx} - H_{yy}}\right) \end{aligned} \quad (17)$$

with the trigonometric formula  $\tan 2\alpha = 2 \tan \alpha / (1 - \tan^2 \alpha)$ . After a selection of the 5% pixels with the highest  $\lambda_-$  value above a reasonable threshold, the median  $\alpha$

of the remaining  $\alpha(x, y)$  values gives the orientation of the spectrum with respect to the  $x$  axis. A linear fit can also be performed across the selected pixels and the slope gives an angle very close to the one estimated with the median of the angle values. This process is illustrated Figure 8.

Note that because of the Atmospheric Differential Refraction (ADR) the spectrogram can be sheared transversally to the dispersion axis. The ADR shear is of the order of  $2''$  across the visible spectrum, which is 5 pixels at CTIO while the spectrogram is  $\approx 700$  pixels long and it is thus neglected at this step of this analysis. On the other hand it will be fully accounted for in the full forward model.

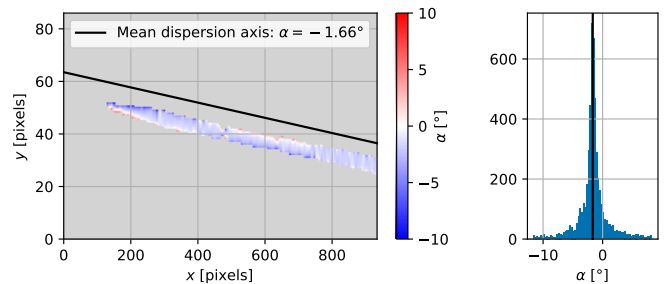


**Fig. 8.** Left: angle  $\alpha$  on the spectrogram image for the 5% pixels with the highest  $\lambda_-$  values found in the Hessian matrix, and dispersion axis as the median of the angles (black line, shifted upward for clarity). The light grey color indicates the masked pixel with low  $\lambda_-$  values. Right: histogram of the selected angles from the left figure, and its median (black vertical line).

### 3.4. Background estimation

The background of the image must be carefully subtracted to avoid bias in the estimation of the spectrum flux and its PSF. However, due to optical vignetting it can be non-flat, and it is dispersed. It can also contain additional field stars and their corresponding spectrograms.

To estimate the spectrogram background, we first select two lateral bands above and below the spectrogram region, of the same length and width  $N_y^{(\text{bgd})}$  (see Figure 9). First we mask the sources detected above a  $3\sigma$  threshold. Then we divide the two lateral regions in a few square boxes of size  $(N_y^{(\text{bgd})}/2, N_y^{(\text{bgd})}/2)$ . The box dimensions must be larger

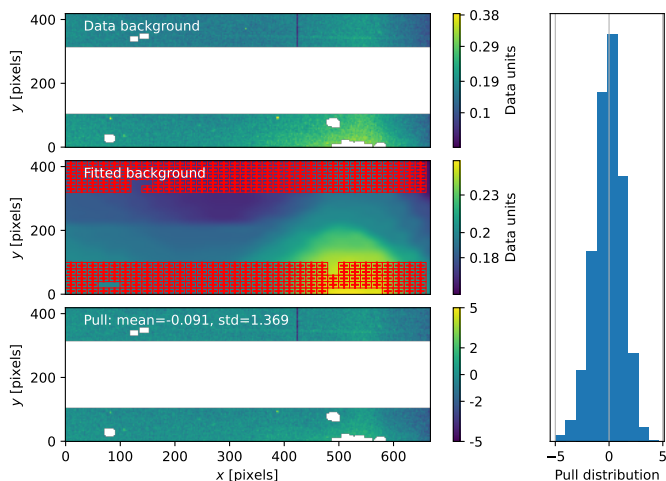


**Fig. 9.** Illustration of the background estimation on a CTIO image (in arbitrary units). *Top*: lateral bands to the spectrogram (masked behind the rectangular grey region) where the background is estimated. The grey patches indicate masked sources. *Middle*: fitted background using the **SExtractor** method with the evaluation boxes in red (here final size is  $20 \times 20$  pixels). *Bottom*: residuals normalised to their uncertainties. *Right*: distribution of the normalised residuals in units of  $\sigma$ .

than the typical size of a field star PSF or of a spectrogram width, but small enough to account for the spatial variations of the background.

To get a first estimate of the background, we use a python wrapper of the **SExtractor**<sup>10</sup> algorithm for background extraction which is roughly based on the bilinear interpolation of the median value inside the boxes, after a sigma-clipping rejection of the outlier pixels (more details in Bertin & Arnouts 1996). This process is illustrated in Figure 9.

In a second step, we analyse the distribution of the background residuals normalised with their uncertainties in the two regions, with the sources being masked. If the histogram of the residuals normalised by their errors (aka the “pull distribution”) departs from a distribution of zero mean and standard deviation equal to 1, we refine the background estimate by dividing the box size by 2 and the process is continued iteratively until the mean is below 1 and the standard deviation is below 2, or until the box size goes below a threshold of 5 pixels.

At the end of this process, the estimated background is interpolated between the two lateral bands to get the background below the spectrogram, and finally subtracted. We call  $B(\mathbf{r})$  the background map. The background RMS is also evaluated by **SExtractor** and is quadratically added as a background uncertainty to the error budget of the spectrogram.

At this stage of the pipeline, with  $\alpha$  and  $\mathbf{r}_0$  given and using a first geometrical wavelength calibration to define roughly the left and right margins of the spectrogram, we can crop the exposure to extract a background subtracted spectrogram. This is extremely useful for diagnosis purposes, and can also be directly studied with an atmospheric forward model (see Section 5).

### 3.5. Spectrum first extraction

The next step of the pipeline we implemented is devoted to the pursuit of the extraction of the first order spectrum  $S_1(\lambda)$  and the estimate of the wavelength dependent PSF. The extraction of the spectral information  $S_1(\lambda)$  from the spectrogram image is a delicate process. The intuitive and traditional way to extract slitless spectra at this stage of the pipeline is to sum over cross-dispersion direction, eventually with weights, to form what we call a cross-dispersion spectrum. Horne (1986) and Robertson (1986) present an optimal method to achieve this. However, this method leads to distorted spectra in case of a wavelength dependent PSF (neighbour wavelengths contaminate each other on the sensor), which is not an issue for spectroscopy but is problematic for spectrophotometry. In the following, we describe first a method to deconvolve the spectrum for the PSF (Section 3.5). The products of that process are then very useful to inform the full forward model finalizing the unbiased extraction of the spectrum (Section 3.8).

#### 3.5.1. Spectrogram first order model

To start with, we consider only the spectrogram of the first diffraction order, potentially with the superposition of a second diffraction order, as provided by the pipeline previous step. The cropped spectrogram has a shape  $(N_x, N_y)$  pixels.

Inspired by equation (7), we model the spectrogram as a discrete stack of  $N_x$  2D PSF realisations of amplitude  $A_i$ , separated by one pixel along the  $x$  axis:

$$I_1(\mathbf{r}|\mathbf{A}, \mathbf{r}_c, \mathbf{P}) = \sum_{i=0}^{N_x} A_i \phi(\mathbf{r}|\mathbf{r}_{c,i}, \mathbf{P}_i) \quad (18)$$

with  $\mathbf{r} = (x, y)$  the vector of the pixel coordinates,  $\mathbf{A}$  an amplitude parameter vector along the dispersion axis of the spectrogram,  $\phi(\mathbf{r}|\mathbf{r}_{c,i}, \mathbf{P}_i)$  the 2D PSF kernel whose integral is normalised to one. This kernel depends non-linearly on a shape parameter vector  $\mathbf{P}_i$  and on a centroid position vector  $\mathbf{r}_{c,i} = (x_{c,i}, y_{c,i})$  where only the  $y_{c,i}$  coordinate is considered unknown. The  $x_{c,i}$  coordinate is set directly to the pixel index  $i$ . This choice of implementation can be discussed and changed, but it was found to be practical since the PSF is then well sampled by the pixel grid. Yet, in theory one could choose another sampling for  $x_{c,i}$ , to increase the speed of the spectrum extraction or try to enhance the spectral resolution.

Somehow, the array of vectors  $\mathbf{r}_c$  is a sampled precursor of the dispersion relation  $\Delta_1(\lambda)$  and the vector  $\mathbf{A}$  is the flux density  $S_1(\lambda)$  integrated within the pixels. If we index all the  $N_x N_y$  spectrogram pixels as a long vector  $\mathbf{Z} = (\zeta_1, \dots, \zeta_{N_x N_y})$ , the equation 18 takes a matricial form:

$$I_1(\mathbf{Z}|\mathbf{A}, \mathbf{r}_c, \mathbf{P}) = \mathbf{M}(\mathbf{Z}|\mathbf{r}_c, \mathbf{P}) \mathbf{A} \quad (19)$$

with

$$\mathbf{M}(\mathbf{Z}|\mathbf{r}_c, \mathbf{P}) = \begin{pmatrix} \phi(\zeta_1|\mathbf{r}_{c,1}, \mathbf{P}_1) & \cdots & \phi(\zeta_1|\mathbf{r}_{c,N_x}, \mathbf{P}_{N_x}) \\ \vdots & \ddots & \vdots \\ \phi(\zeta_{N_x N_y}|\mathbf{r}_{c,1}, \mathbf{P}_1) & \cdots & \phi(\zeta_{N_x N_y}|\mathbf{r}_{c,N_x}, \mathbf{P}_{N_x}) \end{pmatrix} \quad (20)$$

<sup>10</sup> <http://www.astromatic.net/software/sextractor>

The  $(N_x N_y, N_x)$  matrix  $\mathbf{M}$  is called the design matrix.

This model of the spectrogram is designed to deconvolve the spectrum  $S_1(\lambda)$  from the PSF. In principle, one can choose to sample it with PSF kernels separated by arbitrary distances. However, if the PSF is correctly sampled by the pixel grid, it is difficult to extract the spectrum with a spatial resolution below the typical PSF width, and therefore below the pixel size.

Note that at this stage we want to extract the spectrum from a spectrogram potentially contaminated by higher diffraction orders, as yielded by the pipeline steps discussed above, or distorted by atmospheric differential refraction. The final extraction using a full forward model that fully deals with these physical effects is the last step of the **Spectractor** pipeline, presented in section 3.8.

### 3.5.2. Preparation for deconvolution

To initialize the deconvolution with parameters close to the final best model, a first PSF fit is performed transversally to the dispersion axis with 1D PSF kernels on the rotated spectrogram image:

$$\mathbf{I}_1^{(1D)}(\mathbf{r}|\mathbf{A}^{(1D)}, \mathbf{r}_c, \mathbf{P}) = \sum_{i=0}^{N_x} A_i^{(1D)} \phi^{(1D)}(\mathbf{r}|\mathbf{r}_{c,i}, \mathbf{P}_i). \quad (21)$$

This procedure is done in two steps. The first step fits the 1D parameters independently for each pixel column, applying a  $5\sigma$  clipping to reject field stars and other CCD defects. In the second step, a polynomial evolution of the 1D PSF parameter vector along the dispersion axis is proposed. For instance, a polynomial evolution of the  $y_{c,i}(x_{c,i})$  positions can model the transverse ADR and a polynomial evolution of the width of PSF can model a defocusing effect. The polynomial coefficients are fitted using a Gauss-Newton minimisation of a  $\chi^2$  (equation 23) for the non-linear parameters (see appendix B), alternating with a linear resolution for the amplitude parameters as follows.

Assuming that we gather all the spectrogram pixel values in a long vector  $\mathbf{D}$  (as  $\mathbf{Z}$ ), we can model it as:

$$\mathbf{D} = \mathbf{M}(\mathbf{Z}|\mathbf{r}_c, \mathbf{P})\mathbf{A} + \epsilon, \quad (22)$$

with  $\epsilon$  a random noise vector; the  $\chi^2$  function to minimise is:

$$\chi^2(\mathbf{A}|\mathbf{P}) = (\mathbf{D} - \mathbf{M}\mathbf{A})^T \mathbf{W} (\mathbf{D} - \mathbf{M}\mathbf{A}) \quad (23)$$

with  $\mathbf{W}$  the weight matrix of dimension  $(N_x N_y, N_x N_y)$ , inverse of the data covariance matrix (see section 3.1). In most cases this matrix is diagonal as the pixels are considered all independent. The minimum of equation 23 is reached for the set of amplitude parameters  $\hat{\mathbf{A}}$  given by:

$$\hat{\mathbf{A}}^{(1D)} = (\mathbf{M}^T \mathbf{W} \mathbf{M})^{-1} \mathbf{M}^T \mathbf{W} \mathbf{D}. \quad (24)$$

The covariance matrix associated with the  $\hat{\mathbf{A}}$  coefficients is  $\mathbf{C}^{(1D)} = (\mathbf{M}^T \mathbf{W} \mathbf{M})^{-1}$ . At the end of this process, we get a first guess of the  $\mathbf{r}_c$  and  $\mathbf{P}$  parameters, and a first guess of the amplitudes  $\hat{\mathbf{A}}^{(1D)}$  with their uncertainties  $\sigma_{A^{(1D)}}$ , which form what we call a transverse cross-spectrum.

The result of this extraction is illustrated on simulated data in Figure 10 left. For this simulation, we chose to ignore the second order diffraction and we used a wide PSF

kernel with lots of chromatic variations to enhance the visibility of the residuals for the 1D extraction:  $(\gamma_0, \gamma_1, \gamma_2) = (10, 2, 5)$  and  $(\alpha_0, \alpha_1, \alpha_2) = (2, 0, 0)$ . At first glance in the top panel, the model seems accurate but looking at the residuals we see that this 1D model failed to capture the true evolution of the PSF shape with wavelength. As expected, the residuals are less dramatic with a thinner PSF, but remain measurable, demonstrating the need to use a 2D PSF extraction method.

At this stage, we obtained a spectrum close to a cross-dispersion spectrum as in Horne (1986) and Robertson (1986) but informed with a fitted PSF model having a smooth polynomial wavelength evolution.

### 3.5.3. PSF deconvolution

Having provided ourselves with this first 1D estimate of the spectrum, we can resort to a more accurate 2D PSF modelling. When using 2D PSF kernels, the latter linear regression method enters in the category of the deconvolution problems or inverse problems. Since the spectral amplitude information is mixed and diluted at a scale below the typical size of the PSF, the computation of the  $\hat{\mathbf{A}}$  vector sampled at the pixel scale inverting equation 19 using 2D PSF kernels may lead to results far from the reality while giving a seemingly good fit to data (low  $\chi^2$ ). Doing so, a common symptom is the alternation of positive and negative values in  $\hat{\mathbf{A}}$ , or at least with large variations, demonstrating that the problem is ill-posed. As we know by the physics that well-sampled spectra are rather continuous and differentiable functions, we enforce a regularisation method to smooth the resulting  $\hat{\mathbf{A}}$  vector.

A first fit to the data, without any prior on  $\mathbf{A}$ , using a 1D transverse PSF model fitted independently to each column of data along the dispersion axis thus yields a vector  $\hat{\mathbf{A}}^{(1D)}$  containing most of the spectral flux, especially in the smooth parts of the spectrum, but lacking precision in the rapidly varying parts. Indeed, the most visible effect of the PSF is to smooth the absorption lines and more generally to deform the spectral information where the spectral energy density evolves rapidly (for instance in the blue part of the spectrum), while conserving the total flux. It provides nonetheless useful information that we use as a prior  $\mathbf{A}_0$  on  $\mathbf{A}$  when performing a fit using a 2D PSF kernel with a Tikhonov regularisation.

The Tikhonov regularisation method proposes to add a regularisation quantity to the  $\chi^2$  and minimise a new cost function:

$$\begin{aligned} \mathcal{E}(\mathbf{A}|\mathbf{r}_c, \mathbf{P}) &= (\mathbf{D} - \mathbf{M}\mathbf{A})^T \mathbf{W} (\mathbf{D} - \mathbf{M}\mathbf{A}) \\ &\quad + r(\mathbf{A} - \mathbf{A}_0)^T \mathbf{Q} (\mathbf{A} - \mathbf{A}_0) \\ &= \chi^2(\mathbf{A}|\mathbf{r}_c, \mathbf{P}) + r\chi_{\text{pen}}^2(\mathbf{A}|\mathbf{A}_0), \end{aligned} \quad (25)$$

$$\mathbf{A}_0 = \hat{\mathbf{A}}^{(1D)} \quad (26)$$

where  $\mathbf{Q}$  is a weight matrix. The last term favours  $\hat{\mathbf{A}}$  to be close to prior vector  $\mathbf{A}_0$ , with a positive regularisation hyper-parameter  $r$ .

Minimising this  $\mathcal{E}(\mathbf{A}|\mathbf{r}_c, \mathbf{P})$  function is still a linear regression for the  $\mathbf{A}$  parameters, whose optimal value is now:

$$\hat{\mathbf{A}} = (\mathbf{M}^T \mathbf{W} \mathbf{M} + r\mathbf{Q})^{-1} (\mathbf{M}^T \mathbf{W} \mathbf{D} + r\mathbf{Q}\mathbf{A}_0) \quad (27)$$

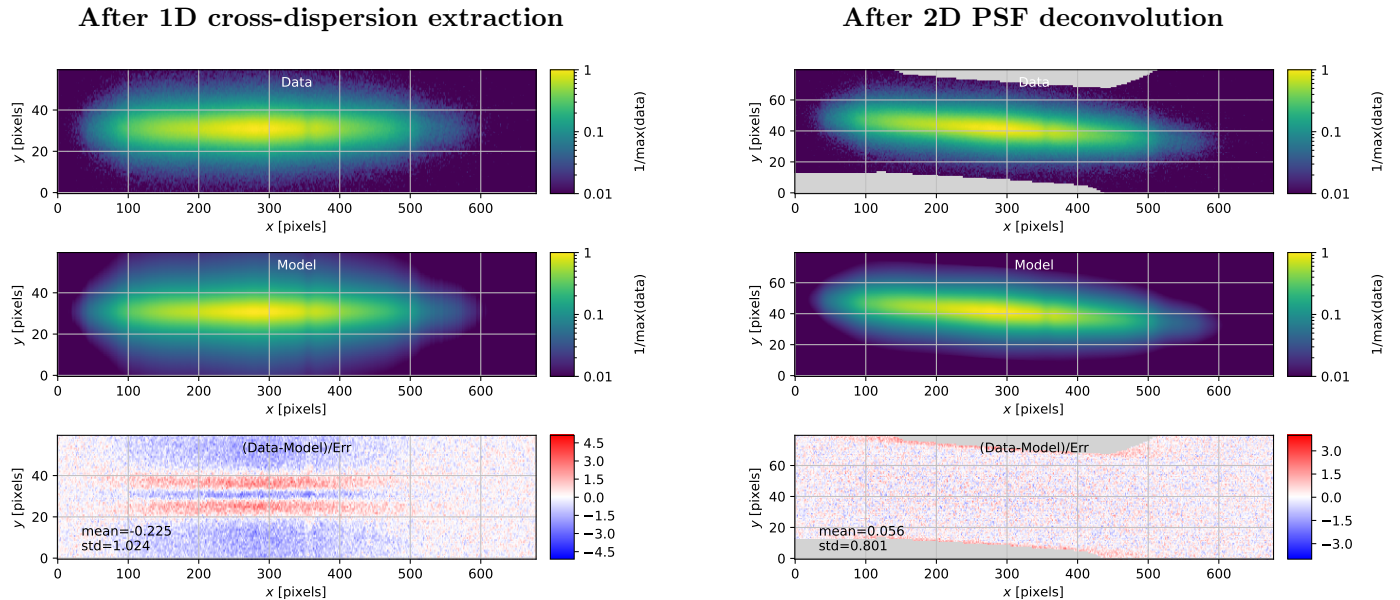


**Fig. 10.** Results from the deconvolution of a simulated spectrogram of HD111980 CALSPEC star with a Moffat PSF kernel, without second diffraction order contamination,  $(\gamma_0, \gamma_1, \gamma_2) = (10, 2, 5)$  and  $(\alpha_0, \alpha_1, \alpha_2) = (2, 0, 0)$ . *Left:* simulated spectrogram (top), best fitting spectrogram model (middle) and residuals in units of  $\sigma$  (bottom) after the rotation process and the 1D transverse fit. *Right:* same simulated spectrogram with its original rotation (top), best fitting spectrogram model (middle) and residuals in units of  $\sigma$  (bottom) after the deconvolution process. All color maps are normalised by the maximum of the simulated spectrogram. Grey areas designate masked pixels.

The covariance matrix associated with  $\hat{\mathbf{A}}$  is directly:

$$\mathbf{C} = (\mathbf{M}^T \mathbf{W} \mathbf{M} + r \mathbf{Q})^{-1} \quad (28)$$

We tested different  $\mathbf{Q}$  matrices on CTIO simulations and the one that gives the most satisfying results when comparing  $\hat{\mathbf{A}}$  to the true amplitudes uses the Laplacian operator  $\mathbf{L}$ :

$$\mathbf{L} = \begin{pmatrix} -1 & 1 & 0 & 0 & \cdots & 0 & 0 \\ 1 & -2 & 1 & 0 & \cdots & 0 & 0 \\ 0 & 1 & -2 & 1 & \cdots & 0 & 0 \\ \vdots & \ddots & \ddots & \ddots & \ddots & \vdots & \vdots \\ 0 & 0 & 0 & 0 & \cdots & -2 & 1 \\ 0 & 0 & 0 & 0 & \cdots & 1 & -1 \end{pmatrix} \quad (29)$$

$$\mathbf{Q} = \mathbf{L}^T \mathbf{U}^T \mathbf{U} \mathbf{L}, \quad (30)$$

with  $\mathbf{U}^T \mathbf{U}$  the matrix proposed in equation C.5:

$$\mathbf{U}^T \mathbf{U} = \begin{pmatrix} 1/\sigma_{A_{1D}^{(1)}}^2 & 0 & \cdots & 0 \\ 0 & 1/\sigma_{A_{1D}^{(2)}}^2 & \cdots & 0 \\ \vdots & \vdots & \ddots & \vdots \\ 0 & 0 & \cdots & 1/\sigma_{A_{1D}^{(N_x)}}^2 \end{pmatrix}. \quad (31)$$

The total variation regularisation is known to be able to retrieve very sharp features (like steps or edges) when deconvolving an image. The Laplacian regularisation can not do the same, but discontinuities are not expected in the physical spectra we are observing. Moreover the norm-2 regularisation offers analytical solution while a norm-1 regularisation needs to conduct an iterative minimisation process (more details in appendix C).

As for the 1D transverse estimate, the deconvolution fit is performed using a Gauss-Newton minimisation of

$\mathcal{E}(\mathbf{A}|\mathbf{P})$  for the non-linear  $\mathbf{P}$  parameters (see appendix B), and a linear resolution for the  $\mathbf{A}$  parameters (see section 3.5.2). The Gauss-Newton minimisation is repeated 3 times with a clipping rejection of bad pixels to remove field stars or CCD defects that can pull the final parameters towards undesired directions. At the end of this process, we get the measured  $\hat{r}_c$  and  $\hat{\mathbf{P}}$  parameters, and a measurement of the amplitudes  $\hat{\mathbf{A}}(r)$  with their covariance matrix  $\mathbf{C}(r)$ , which form what we can call a spectrum, eventually contaminated by the second diffraction order. To accelerate the computation, regions farther than two times the PSF FWHM from the centroids are masked and set to zero with null weights (grey regions in Figure 10). For this process, a default value of the  $r$  regularisation parameter as been chosen, without fully exploring how it could be optimised.

The PSF deconvolution problem was tackled in another way in Ryan et al. (2018) for slitless spectroscopy. Instead of using a PSF model, the mathematical model is inverted using multiple exposures of the same spectrum ideally taken at different orientations, dispersion directions, or dithered positions. Doing so the amount of data leads to an invertible problem, but still needs a damping hyper-parameter equivalent to  $r$  introduced in equation 25. In Ryan et al. (2018), the tuning of this hyper-parameter is performed manually finding the breaking point of a specific L-curve (see Hansen 1992). This method is mathematically close to the one we used (described in Section 3.5.4) as it leads to an equilibrium between information coming from the prior and data.

### 3.5.4. Optimisation of the regularisation

What is the right amount of information searchable in the data? It is first reasonable to think that it is hopeless to find information at a spatial scale below the typical width of the

convolution kernel with a unique spectrogram. Therefore, what is the way to find the optimal hyper-parameter  $r$  ?

The optimisation of the regularisation parameter  $r$  is performed via the study of the resolution operator

$$\mathbf{R} = \mathbf{I} - r\mathbf{CQ} \quad (32)$$

with  $\mathbf{I}$  the identity matrix. A fruitful interpretation of the  $\mathbf{R}$  operator is given in Hansen (2010) with

$$\begin{aligned} \text{Tr } \mathbf{I} &= \text{Tr } \mathbf{R} + \text{Tr } (r\mathbf{CQ}) \Leftrightarrow \\ [\# \text{ parameters}] &= [\# \text{ parameters resolved by data}] \\ &+ [\# \text{ parameters resolved by prior}], \end{aligned} \quad (33)$$

where the trace of the resolution operator gives the effective number of degrees of freedom that can be extracted from the data for a given amount of prior information. We set

$$N_{\text{dof}} = \text{Tr } \mathbf{R}. \quad (34)$$

The optimal  $r$  parameter is found minimizing the following  $G(r)$  function, which behaves like a reduced  $\chi^2$ :

$$G(r) = \frac{\chi^2(\hat{\mathbf{A}}|\hat{\mathbf{r}}_c, \hat{\mathbf{P}})}{(N_x N_y - N_{\text{dof}})^2}. \quad (35)$$

This method, known as General Cross-Validation (GCV), is extensively presented in e.g., Golub et al. (1979); Wahba (1990); Hansen (2010). It is demonstrated that the minimum of  $G(r)$  corresponds to the minimum of the distance  $|\mathbf{M}\hat{\mathbf{A}} - \mathbf{M}\mathbf{A}_{\text{truth}}|^2$  where  $\mathbf{A}_{\text{truth}}$  is the true amplitude vector hidden in the data.

We tested different ways to implement the optimisation of the regularisation process in `Spectractor`. The one that gives the most efficient result (in terms of rapidity and bias of the final result) is to set a default reasonable regularisation parameter for the fitting procedure of the amplitude  $\hat{\mathbf{A}}$  and PSF  $\hat{\mathbf{r}}_c$ ,  $\hat{\mathbf{P}}$  parameters, and finally to find the minimum of the  $G(r)$  function. We observed on simulations that whatever  $r$  hyper-parameter is chosen at the beginning, the process reconstructs an unbiased spectrum at the end of the  $\mathcal{E}(\mathbf{A}|\mathbf{r}_c, \mathbf{P})$  minimisation. The level of regularisation of the solution can thus be set *a posteriori* by finding the optimal  $r$  after minimizing the  $G(r)$  function.

The result of a 2D deconvolution process is presented in Figures 10 right panel for a simulation with a wide PSF kernel but without second diffraction order to stress the benefit of the deconvolution. The residual map between the best-fitting model and the simulated spectrogram shows that the 1D transverse fit can not extract correctly the spectrum from the spectrogram image (Figure 10 left), while the 2D deconvolution ends with a quasi unstructured residual map respecting the expected Gaussian distribution (Figure 10 right). As our model is informed by a PSF model, we are able to extract spectra with a single exposure involving rather small matrices compared with Ryan et al. (2018). This allows us to tune the  $r$  hyper-parameter automatically in a few seconds with a standard laptop.

If the spectrogram is not fully contained in the sensor area, the spectrum exhibits a discontinuity which makes the norm-2 regularisation fail (second derivative from the Laplacian operator is undefined). Then, for a given instrumental PSF, it is better to use a more dispersive grating to feed the deconvolution with more data and increase the wavelength resolution, but the spectrogram must fit inside the sensor area to use regularisation techniques.

### 3.5.5. The spectrophotometric uncertainty principle

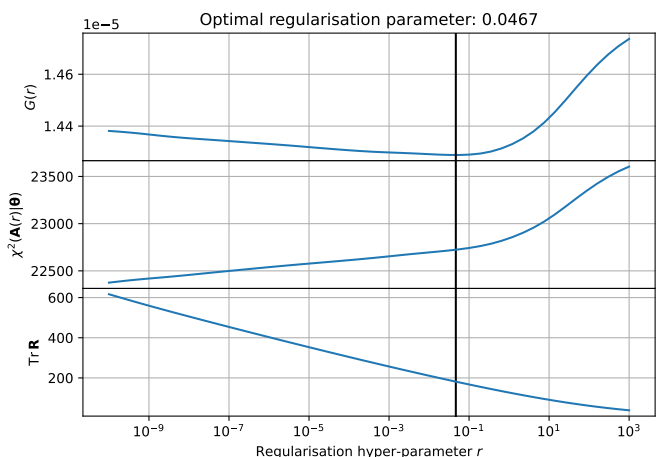


**Fig. 11.** Optimisation of the  $r$  hyper-parameter for a simple simulation with  $n_{\text{PSF}} = 0, \gamma_0 = 5, \alpha_0 = 3$  (and same characteristics as in Table 1). *Top:* the  $G(r)$  function (blue) and the minimum position  $r = 0.0467$  (black vertical line). *Middle:*  $\chi^2$  evolution with  $r$ . *Bottom:* trace of the resolution matrix  $\text{Tr } \mathbf{R}$ . The intersection with the black line gives the effective number of parameters fitted by data, here 180.

The regularity of the deconvolved solution depends on the hyper-parameter  $r$ . The optimal  $r$  parameter is chosen as the minimum of the  $G(r)$  function represented on the top panel of Figure 11 for a simple simulation with  $n_{\text{PSF}} = 0, \gamma_0 = 5, \alpha_0 = 3$  (and same characteristics as in Table 1):

$$\phi(x, y|\mathbf{r}_c, \mathbf{P}) = \frac{\alpha_0 - 1}{\pi\gamma_0^2} \left[ 1 + \left( \frac{x - x_c}{\gamma_0} \right)^2 + \left( \frac{y - y_c}{\gamma_0} \right)^2 \right]^{-\alpha_0}. \quad (36)$$

The second panel displays the  $\chi^2(\hat{\mathbf{A}}(r)|\hat{\mathbf{r}}_c, \hat{\mathbf{P}})$  function which shows that the optimal  $\mathbf{A}(r)$  solution is not the one minimizing the agreement with data (minimum  $\chi^2$ ) but the one that makes a compromise with a regularisation scheme (modelled by the  $\chi_{\text{pen}}^2(\mathbf{A}|\mathbf{A}_0)$  penalty term). The lower panel illustrates that the effective number of amplitude parameters fitted by data with the optimal regularisation hyper-parameter is approximately of 180. Note that for this simulation, around 680 amplitude parameters were fitted in a spectrogram built with a constant PSF FWHM of around 5.5 pixels. Intuitively, we can conjecture that there must exist an optimal relationship between the typical width of the PSF kernel and the amount of information that is searchable in data:

$$\begin{aligned} [\text{PSF width}] \times [\# \text{ effective degrees of freedom}] \\ \approx [\# \text{ parameters}]. \end{aligned} \quad (37)$$

If the number of searched parameters is too high, the problem becomes ill-posed. If it is too low, then one should compensate with a wide PSF kernel. We thus postulate that we should have a spectrophotometric uncertainty principle of the type:

$$\sigma_{\text{PSF}} \times \frac{N_{\text{dof}}}{N_x} \gtrsim h \quad (38)$$

where optimum is reached at equality and  $h$  is a number with the same units as  $\sigma_{\text{PSF}}$  the width of the PSF kernel. This formula gives the minimum number of degrees of freedom to describe data, given a PSF width.

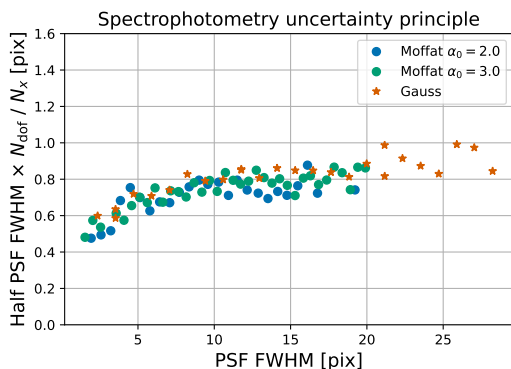


**Fig. 12.** Product of the PSF FWHM with  $N_{\text{dof}}/N_x$  as a function of the PSF FWHM for three different PSF models: a Gaussian kernel (orange stars), a Moffat kernel with  $\alpha_0 = 2$  (blue points) and a Moffat kernel with  $\alpha_0 = 3$  (green points).

We tested the deconvolution and regularisation process on a large number of simulated spectrograms of constant width ( $n_{\text{PSF}} = 0$ ), but without second diffraction order, for the sake of simplicity without any loss of generality. We tried a Gaussian PSF kernel, as well as a Moffat kernel with two different exponents ( $\alpha_0 = 2$  and  $3$ ) and various  $\gamma_0$  values. The results are summarised in Figure 12. For the three models,  $\sigma_{\text{PSF}}$  was chosen to be half of the PSF FWHM. The figure shows that for any PSF kernel the measure of the number of degrees of freedom  $N_{\text{dof}}/N_x$  scales as the inverse of the PSF width. They show a definite trend for the product  $\sigma_{\text{PSF}} \times N_{\text{dof}}/N_x$ , that appears to be asymptotically constant and equal to a number  $h$  close to 0.8 pixel when the PSF size is significantly greater than a few pixels. This  $h$  value varies with the signal-to-noise ratio of the spectrogram, but for a situation it locks the relationship between  $\sigma_{\text{PSF}}$  and  $N_{\text{dof}}$ . This flatness of the relationship shows that our procedure is in agreement with considering as optimal the extraction of information at the scale of the PSF kernel.

It is also noteworthy that this equation could be exploited to accelerate the computation of the PSF cubes: instead of computing a PSF kernel for each pixel column  $i$ , we could compute it for each  $N_{\text{dof}}/N_x$  pixel. As the computation times were not an issue in this paper, we left this investigation for a future project were computation speed counts.

### 3.6. Wavelength calibration

Despite the astigmatism of the system, in first approximation the slitless spectrograph obeys to the usual grating formula (Eq. 1, see e.g., Murty 1962; Hall 1966; Schroeder & Inc 2000). Using the notations of Figure 1, the grating formula can be inverted to find the relation between the  $u$  coordinate along the dispersion axis and  $\lambda$ .

First, we assume that the true 0th order position is at  $u_0$  along the dispersion axis, but that a misfit of its centroid (see Section 3.2) can shift the position by a quantity  $\delta u_0^{(\text{fit})}$ .

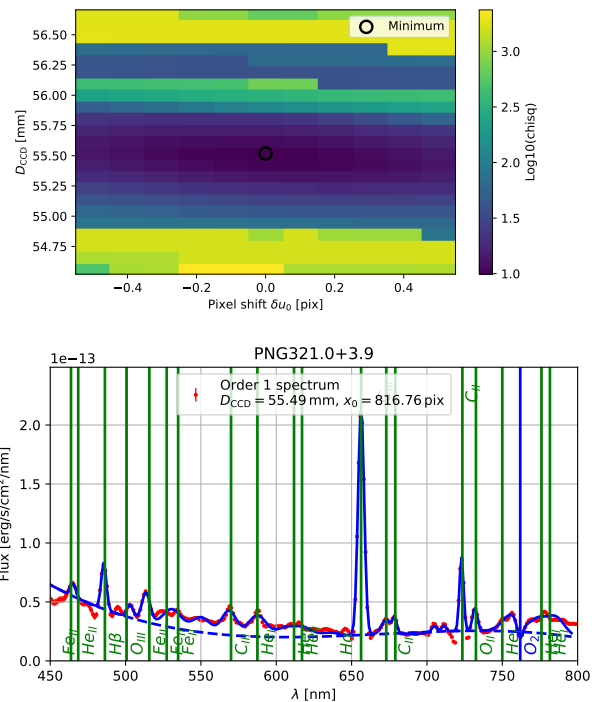


**Fig. 13.** *Top:* global  $\chi^2(\delta u_0^{(\text{fit})}, D_{\text{CCD}})$  function and its minimum (black circle) for planetary nebula PNG321.0+3.9 observed at CTIO: the sharp steps on top of the plot are due whether certain lines are detected or not. *Bottom:* calibrated spectrum of PNG321.0+3.9. Vertical lines indicates emission or absorption lines that are detected, positioned at their tabulated values. The dashed blue lines is the fitted background (whose degree depend on its length) and the plain blue lines are the Gaussian profiles fitted on data.

The ADR also slightly spreads the order 0 image along the local constant azimuth line in a deterministic way depending on the airmass and the spectrum of the source. It also depends on the parallactic and camera angles, the atmosphere temperature, pressure and humidity. It is incorporated in the wavelength calibration process as a wavelength dependent shift  $\delta u^{(\text{ADR})}(\lambda)$  of the PSF centroid position along the dispersion axis with respect to a reference wavelength  $\lambda_{\text{ref}}$ :  $\delta u^{(\text{ADR})}(\lambda_{\text{ref}}) = 0$ .

We model this effect using the NIST metrology toolbox<sup>11</sup> recommendation of using a modified version of the Edlén equation (Edlén 1966) by Birch and Downs (Birch & Downs 1993; Birch & Downs 1994) (see appendix D).

The distance  $d(\lambda)$  between an abscissa of the spectrogram and the zeroth order then reads:

$$\delta u(\lambda) = \delta u_0^{(\text{fit})} + \delta u^{(\text{ADR})}(\lambda), \quad (39)$$

$$u_0 = D_{\text{CCD}} \tan \theta_0, \quad (40)$$

$$d(\lambda) = u(\lambda) - u_0 - \delta u(\lambda), \quad (41)$$

so:

$$d(\lambda|D_{\text{CCD}}, \delta u_0^{(\text{fit})}) = D_{\text{CCD}} [\tan(\arcsin(pN_{\text{eff}}\lambda + \sin \theta_0)) - \tan \theta_0] - \delta u^{(\text{ADR})}(\lambda) - \delta u_0^{(\text{fit})}. \quad (42)$$

<sup>11</sup> <https://emtoolbox.nist.gov/Wavelength/Documentation.asp>

The bijection between the position on the CCD and the wavelength is thus parametrised with two unknown parameters,  $D_{\text{CCD}}$  and  $\delta u_0^{(\text{fit})}$ , that need to be fitted.

As a starting point, we compute a first wavelength array  $\lambda_0$  from the array of distances  $d$  to the order 0 along the dispersion axis, assuming  $\delta u_0 = 0$  and given a prior value of  $D_{\text{CCD}}$ . To get a wavelength array given  $D_{\text{CCD}}$  and  $\delta u_0$ , equation 42 is inverted as

$$\lambda = \frac{1}{pN_{\text{eff}}} \left[ \sin \arctan \left( \frac{d + \delta u^{(\text{ADR})}(\lambda) + \delta u_0^{(\text{fit})}}{D_{\text{CCD}}} \right) - \sin \theta_0 \right]. \quad (43)$$

To get rid of the ambiguity with ADR which depends also on wavelength, we iterate this computation 5 times starting from  $\lambda_0$  and updating  $\lambda$ . We checked that it is enough to converge toward a stable wavelength solution. At those steps, we have associated a wavelength array  $\lambda$  with the amplitude array  $\mathbf{A}$ . From this calibration,  $\lambda_{\text{ref}}$  is computed as the mean wavelength weighted by the spectrum  $\mathbf{A}$  itself.

The parameters  $D_{\text{CCD}}$  and  $\delta u_0^{(\text{fit})}$  are fit on data using the most prominent absorption (or emission) lines on the observed stellar spectrum (typically the hydrogen lines  $H\alpha$  and  $H\beta$ , and the dioxygen lines at 762.1 nm and 686.7 nm). They are locally fitted with a polynomial background plus a Gaussian profile of unknown height, centroid and width. A partial  $\chi^2$  quantity is computed for each spectroscopic line, and added into a global  $\chi^2$ .

A penalty defined as the squared distance between the fitted Gaussian centroids and the tabulated values for the detected lines, weighted by the squared signal-to-noise ratio, is then added to the  $\chi^2$ .

Finally, the full  $\chi^2$  and its penalty are normalised to the number of detected lines. This normalisation of the global  $\chi^2$  is necessary to avoid solutions that favour a lower number of detected lines, while the penalty gives more weights to the well detected lines and anchors them on their tabulated values. The two parameters  $\delta u_0^{(\text{fit})}$  and  $D_{\text{CCD}}$  are varied to minimize the penalised global  $\chi^2$  and find the best solution for the wavelength calibration.

The result of this process is illustrated on Figure 13. On top, the global  $\chi^2$  is represented for the wavelength calibration of planetary nebula PNG321.0+3.9 observed at CTIO. The sharp steps at high or low  $D_{\text{CCD}}$  values reflects situations where some emission lines are detected or not, which emphasizes the need to normalise the global  $\chi^2$  by the number of detected lines. The smoothness around the minimum is due to the penalty term on  $\delta u_0^{(\text{fit})}$ . In the calibrated spectrum, we can observe many emission lines that have been detected by the algorithm, and a good alignment between the tabulated values (represented by the vertical lines), the extrema of the Gaussian profiles and those of the data curve.

### 3.7. Flux calibration

With the fitted wavelength solution, the spectrum amplitude  $\hat{\mathbf{A}}$  can be converted from ADU units to flux densities in  $\text{erg/s/cm}^2/\text{nm}$ , assuming that the telescope collecting area  $S_T$ , the exposure time  $\tau$  and the CCD gain  $G_{\text{CCD}}$  (in  $e^-/\text{ADU}$ ) are known:

$$S_1(\lambda) = \hat{\mathbf{A}} \times \frac{hc G_{\text{CCD}}}{S_T \tau \lambda \delta \lambda}, \quad (44)$$

**Table 2.** Emission lines detected in the planetary nebula PNG321.0+3.9 spectrum with a signal-to-noise ratio (SNR) above 10. The third column gives the centroid of the fitted Gaussian profile and the fourth column the distance with the tabulated value. The equivalent width (EQW) is reported in the last column.

Line	Tabulated nm	Detected nm	Shift nm	FWHM	Amplitude $\text{erg/s/cm}^2/\text{nm}$	SNR	EQW nm
$He_I$	388.8	383.8	-5.0	14.1	1.1e-13	46.0	-28.3
$H\beta$	486.3	485.6	-0.7	4.0	3.9e-14	17.1	-3.0
$Fe_{II}$	515.8	513.6	-2.2	6.5	2.5e-14	10.9	-9.6
$H\alpha$	656.3	656.3	-0.0	4.8	1.9e-13	84.6	-44.5
$C_{II}$	723.5	722.9	-0.6	3.2	6.4e-14	28.0	-7.1
$He_I$	861.7	865.6	3.9	8.7	5e-15	10.2	-2.5
$C_{III}$	970.5	968.8	-1.7	6.4	1.1e-14	22.9	-1.5
$He_I$	1023.5	1024.3	0.8	10.4	5.6e-15	13.2	-4.7

where  $\delta\lambda$  is the local variation of  $\lambda$  within one pixel.

The end product of this pipeline is thus a background-subtracted spectrum, calibrated in wavelength and flux, which is the product of three quantities: the object SED, the instrumental transmission and the atmospheric transmission, potentially contaminated by a second diffraction order, since this later hasn't yet been taken into account.

### 3.8. Spectrogram full forward model

At the end of the previous steps, we also have in hands a first estimate of the two instrumental model functions  $\phi_1(\mathbf{r}, \lambda)$  and  $\Delta_p(\lambda)$  together with geometric parameters like the zeroth order position  $\mathbf{r}_0$  and the dispersion angle  $\alpha$ . With all these ingredients, we can implement a full forward model of the data, also taking into account the atmospheric differential refraction (ADR) and the superimposition with the second diffraction order (last stage of Figure 3).

In practice, we enrich the forward model described in the steps above with the knowledge of the ADR physics (see Sections 3.6 and D) and with the knowledge of the second order to first order transmission ratio  $r_{2/1}(\lambda)$  of the spectrograph disperser. The ADR model replaces a polynomial approach to predict  $\Delta_p(\lambda)$ . In other words, it is used to predict the trace of the spectrogram on the sensor with no free parameter, as long as airmass, outside pressure, outside temperature and humidity are given. With that, two free parameters remain in order to fully constrain the spectrogram trace on the sensor: the dispersion axis angle  $\alpha$  and  $\delta y^{(\text{fit})}$  that compensates a misfit of the zeroth order centroid along the  $y$  axis, and the ratio  $r_{2/1}(\lambda)$  which can be measured on an optical test bench (see Section 5.1) or on-sky data. In the full forward model, we use a new design matrix  $\tilde{\mathbf{M}}$  defined as:

$$\tilde{\mathbf{M}} = \mathbf{M}(\mathbf{Z}|\mathbf{r}_c, \mathbf{P}) + A_2 \mathbf{R}_{2/1} \mathbf{M}(\mathbf{Z}|\mathbf{r}_c^{p=2}, \mathbf{P}^{p=2}), \quad (45)$$

where  $A_2$  is a ‘‘safety’’ normalisation parameter,  $\mathbf{R}_{2/1}$  is the transmission ratio vector computed for a given wavelength calibration,  $\mathbf{r}_c^{p=2}$  are the centroid positions of the second diffraction order PSF kernels and  $\mathbf{P}^{p=2}$  their shape parameters. The vector  $\mathbf{r}_c^{p=2}$  is computed using the grating formula 1 and the ADR model.  $\mathbf{P}^{p=2}$  can be fitted independently of  $\mathbf{P}^{p=1}$  but we chose to assume that the PSF shape depends more on the spectrograph defocusing towards the infrared than on the atmospheric chromatic seeing. The PSF shape parameters for the second diffraction order are thus considered the same than for the first diffraction order at the same distance of the order 0. We

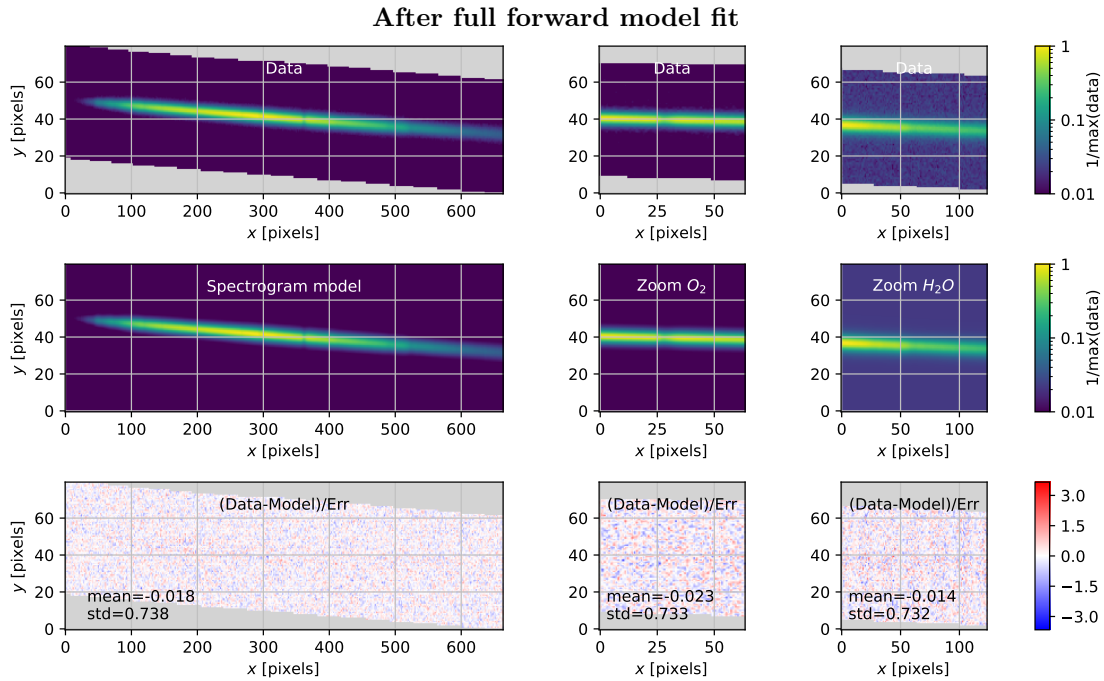


**Fig. 14.** Same as Figure 10 but with the addition of a second-order diffraction spectrogram and after the full forward model fitting procedure.

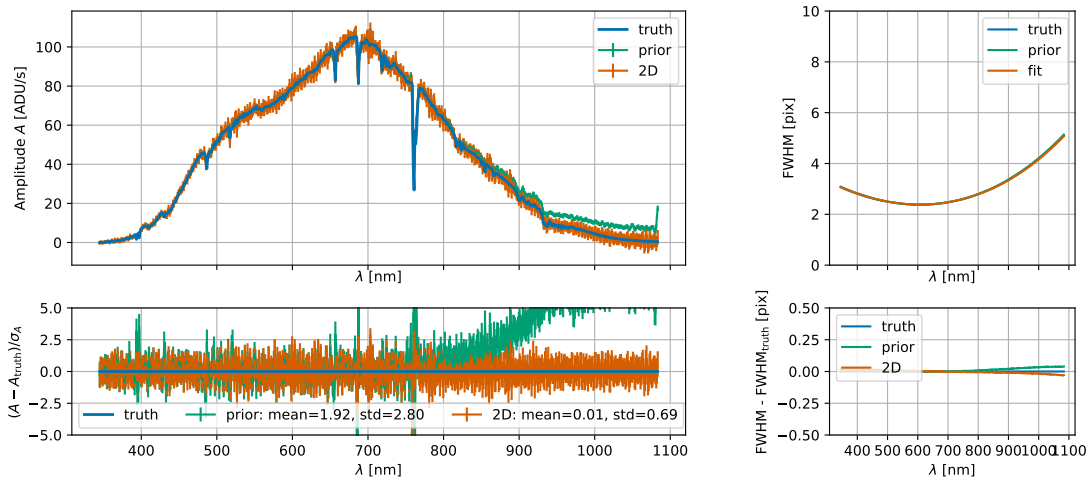


**Fig. 15.** Results from the full forward model fit of a simulated spectrogram of HD111980 CALSPEC star with a Moffat PSF kernel. A second diffraction order was simulated. *Top left:* spectrum output from the full forward model process (orange) compared with the true spectrum injected in the simulation (blue) and the intermediate 1D transverse fit used as the prior vector  $\mathbf{A}_0$  (green). *Bottom left:* residuals between the true spectrum and the 1D and 2D fits normalised by their estimated uncertainties. *Top right:* FWHM of the true PSF (blue, right below the green curve) compared with the fitted PSF during the full forward model procedure (green) or the 1D transverse fit (orange). *Bottom right:* difference between the true PSF FWHM injected in the spectrogram simulation and the 1D and 2D fits. All blue curves are covered by the orange curves.

chose to set the  $\mathbf{P}^{p=2}$  vector accordingly<sup>12</sup>. Therefore, the full forward model now includes both first and second order

spectrogram models as:

$$\mathbf{I}_1(\mathbf{Z}|\mathbf{A}, \mathbf{r}_c, \mathbf{P}) + \mathbf{I}_2(\mathbf{Z}|\mathbf{A}, \mathbf{r}_c^{p=2}, \mathbf{P}^{p=2}) = \tilde{\mathbf{M}} \mathbf{A}. \quad (46)$$

<sup>12</sup> Another choice could have been to assume that the spectrograph does not suffer from defocus, and thus arguing that the PSF shape parameters for the second diffraction order are the same than that of the first diffraction order at the same wavelength whatever the distance to the order 0. For CTIO images, our first choice leads to better fits to data.

We implemented a two steps iterative method, alternating the wavelength calibration described in Section 3.6 and the full forward model described just above (combining a linear fit for the  $\mathbf{A}$  spectrum amplitudes and a Gauss-Newton descent for the non-linear parameters  $\mathbf{P}$ ) with the same  $r$  hyper-parameter that was fitted (in Section 3.5.4).

The  $\mathbf{A}$  parameter vector determined with PSF 2D deconvolution previously (Section 3.5.3) is seeded in the forward model fit as a new prior  $\mathbf{A}_0$ . A  $20\sigma$  clipping is performed to reject the field stars and their concomitant spectrograms as well as other sensor defects. This procedure ensures that all the forward model parameters are fitted again together on data, using the more complete model including  $\mathbf{A}$ ,  $\mathbf{P}$ ,  $D_{\text{CCD}}$ ,  $\delta u_0^{(\text{fit})}$  and  $A_2$ . Their values replaced all the ones that were fitted previously. The residual map obtained is flatter than before, with an even smaller final  $\chi^2$ , and a consequently better accuracy of all the parameters fitted.

The two main products of this step are a first order diffraction spectrum  $S_1(\lambda)$  separated from the second order spectrum, and the second order spectrum  $S_2(\lambda)$  with

$$S_2(\lambda) = r_{2/1}(\lambda)S_1(\lambda), \quad (47)$$

in  $\text{erg/s/cm}^2/\text{nm}$  (following formula (44)).

It is as this point worthwhile to reconsider the second diffraction order not as a nuisance but as a useful signal. With a strong bending due to ADR (for instance with the dispersion axis orthogonal to the zenith direction), it can be detached from the first diffraction order on purpose to maximize the statistical power of the exposure.

In summary, a full forward model takes advantage of the higher diffraction orders as a redundant piece of data to fit all parameters, especially in the bluer part where absorption lines are twice wider in pixels than in the first order spectrum. This is a key advantage of the forward approach on the direct approach.

### 3.9. Validation on simulations

**Table 3.** Parameters of a spectrogram simulation and **Spectractor** estimations, recovered with a full forward model approach.

Parameter	Simulation value	Recovered value
$x_0$ [pix]	743.89	743.76
$y_0$ [pix]	682.92	682.93
$\delta y^{(\text{fit})}$ [pix]	0	$-0.199 \pm 0.003$
$\alpha$ [°]	$-1.5653$	$-1.5654 \pm 0.0004$
$\langle B(\mathbf{r}) \rangle$ [ADU/s]	0.1930	0.1930
$D_{\text{CCD}}$ [mm]	56.322	56.329
$A_2$	1	$0.98 \pm 0.02$
$\gamma_0$	3	$3.00 \pm 0.01$
$\gamma_1$	1	$0.99 \pm 0.02$
$\gamma_2$	1	$1.02 \pm 0.02$
$\alpha_0$	3	$3.01 \pm 0.01$
$\alpha_1$	0	$-0.02 \pm 0.01$
$\alpha_2$	0	$0.03 \pm 0.02$
$N_{\text{dof}}$	669	298
Reduced $\chi^2$	–	0.53

**Notes.** Parameters with uncertainties are fitted during the Gauss-Newton descent of the full forward model, while others are just estimated on data. The simulation was done with a spectrum made from 669 amplitude parameters, and the regularisation process recovered 303 of them. The  $\delta y^{(\text{fit})}$  centroid correction is included in the  $y_0$  quoted value.

To test the full forward model, we simulated a spectrogram with a second diffraction order and a sharp Moffat PSF kernel to increase the spectral resolution (see the PSF

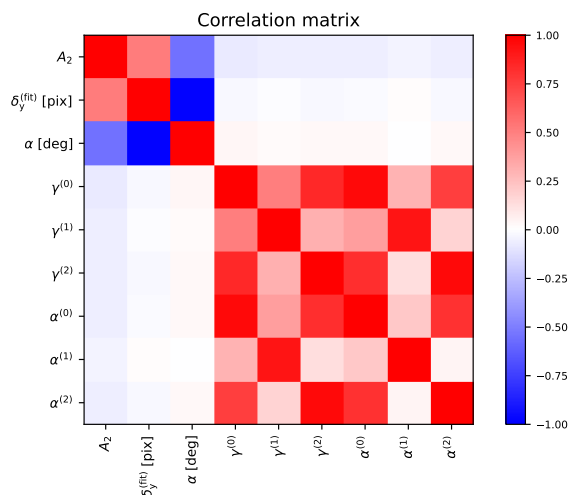


**Fig. 16.** Correlation matrix of the full forward model fitting a spectrogram simulation at the end of the Gauss-Newton descent.

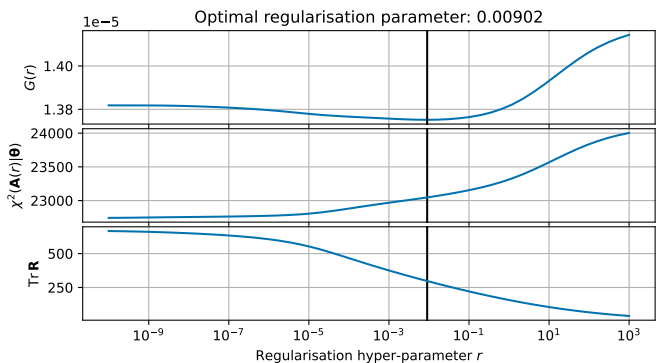


**Fig. 17.** Same as Figure 11 but for the simulation illustrated in Figure 15.

parameter values in Table 3), whose shape evolves as a second order polynomial function. Figure 14 compares simulated data with the fitted spectrogram model, focussing on some atmospheric absorption lines: the residuals follow the expected Gaussian distribution again, even in those fast varying regions of the spectrum.

In Figure 15, we show that the process recovered the true spectrum injected in the simulation within the estimated uncertainties (diagonal elements from the  $\mathbf{C}$  matrix from equation 28). The agreement is excellent at all wavelengths, even around the fast varying absorption lines. On the right panel of the figure, the FWHM of the true PSF is also represented, showing that the reconstructed PSF displays the same wavelength-dependent PSF FWHM as the simulated one. It is also remarkable that while the cross-spectrum issued from the transverse 1D fit described in Section 3.5.2 failed to recover the true spectrum and the true PSF profile because of the presence of the second diffraction order (orange curves), it still proved to be an important seed for the regularisation process, since only its regularity is used thanks to the Laplacian operator  $\mathbf{L}$ .

The recovered parameters are compared with the simulation values in Table 3. They are fitted together with their uncertainties in the full forward model minimisation, which

provides their full covariance matrix (Figure 16), while the other parameters like the star centroid are just estimated on data.

The regularisation quantities are given in Figure 17. We see once again that for a PSF FWHM between 2 to 4 pixels we obtain  $N_{\text{dof}} \approx 300$  out of  $\approx 700$  parameters, confirming the rule of thumb given by the spectrophotometric uncertainty principle. For spectrograms like the ones presented in the previous figures, the end-to-end pipeline takes 2 minutes on a standard laptop.

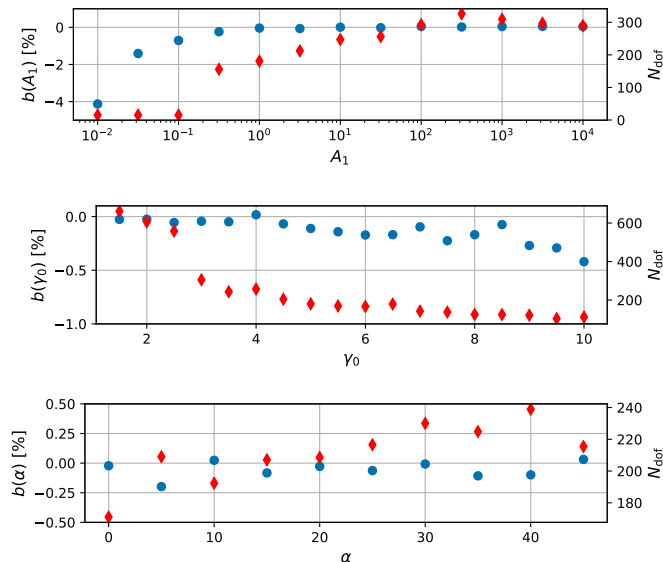


**Fig. 18.** Extraction bias  $b$  (blue points), as a function of the signal-to-noise ration materialized by the amplitude  $A_1$  factor (top), of the PSF width  $\gamma_0$  (middle) and of the rotation angle  $\alpha$  (bottom). For completeness, the effective number of degrees of freedom  $N_{\text{dof}}$  is represented with red diamonds for each simulation.

The **Spectractor** implementation has been tested on many simulations and recovered the simulation parameters within the estimated uncertainties (68% confidence interval) for sets of parameters not too extreme (smooth wavelength dependence of the PSF, PSF kernel sampled over a few pixels). We also evaluated the extraction bias  $b$  between the true spectrum given in the simulation  $S_1^{\text{truth}}(\lambda)$  and the extracted spectrum  $S_1(\lambda)$  as

$$b = \frac{\int d\lambda (S_1(\lambda) - S_1^{\text{truth}}(\lambda))}{\int d\lambda S_1^{\text{truth}}(\lambda)}. \quad (48)$$

The extraction bias was evaluated with many simulations in different cases in terms of signal-to-noise ratio, resolution and geometry. For the first case, the signal-to-noise ratio variation was simulated by multiplying the simulated spectrum by an arbitrary grey factor  $A_1$ , keeping the image background at the same level. The signal-to-noise ratio of the simulation presented Figure 15 and Table 3 corresponds to  $A_1 = 1$ . We found no significant bias in the  $A_1 > 1$  regime (Figure 18) but a small bias appears for lower signal-to-noise spectrograms at the percent level, coming from the assimilation of the Poisson noise as a Gaussian noise in the evaluation of the uncertainty map (see 3.1). The spectrogram resolution variation was simulated changing the

PSF width  $\gamma_0$  and we see small negative bias appearing for low resolution spectra (large  $\gamma_0$ ). Indeed, the latter exhibit wider and shallower absorption lines than the true spectrum which lead to these negative  $b$  values, although at the sub-percent level. However, except for the absorption lines, the overall spectrum shape from blue to red is perfectly recovered. Finally, geometry variations were also simulated using different dispersion axis angles  $\alpha$  and found no bias. In conclusion, the most paramount condition to extract unbiased spectra from slitless spectrophotometry is a sufficient signal-to-noise ratio, closely followed by a sufficiently fine spectral resolution. The adequacy of those parameters being easy to test a priori with forward model simulation.

For completeness, we represented the reconstructed number of degrees of freedom for all these simulations in Figure 18. As expected, for very low signal-to-noise spectrograms this number is close to zero and the extracted spectra provide only from the 1D extraction; but if the signal increases then  $N_{\text{dof}}$  strongly increases until it saturates because of pixelisation. Conversely, this number decreases when the PSF width increases because the spectrogram has a lower spectral resolution.

#### 4. Spectra extraction on data

The success of the spectrum extraction on data depends mostly on the model of the wavelength dependent PSF of the telescope. If the PSF model correctly represents the reality, the residuals after the spectrogram full forward model fit converges towards the expected Gaussian distribution. Otherwise, the extracted spectrum is distorted were the PSF is too far from reality.

This is illustrated on Figure 19. On the left panels, a blazed Thorlabs grating 300 lines/mm was chosen to observe CALSPEC star HD111980 at CTIO on 2017, May 30th. This grating, directly placed in the filter wheel at  $D_{\text{CCD}} \approx 55$  mm from the CCD presents a rather strong defocusing that is not well modelled by our default circular Moffat PSF, even with an order 4 polynomial evolution with wavelength.

The building of an appropriate model for these highly defocused PSF is left for a future work, and is presented here as an illustration to how much the prior understanding of the telescope can be worthwhile in a forward fitting approach. Those extractions used a sigma clipping procedure with a  $20\sigma$  threshold, in order to reject only the field stars and not the poorly modelled spectrogram pixels.

However, the same PSF kernel used to treat the same star observed 5 minutes later but with an amplitude hologram optimised to correctly focus the spectrogram at all wavelength (Moniez et al. 2021) leads to residuals between  $\pm 5\sigma$  (right figures), mostly dominated by a field star contaminating the spectrogram around 530 nm.

Parameters of interest for those two extractions are summarised in Table 4. We realised *a posteriori* that the signal to noise ratio was not sufficient to fit  $A_2$ , and decided to keep it fixed at 1. The way the ratio  $r_{2/1}(\lambda)$  was obtained for these exposures is explained in Section 5.

The calibrated spectra given by **Spectractor** at the end of the extraction process are given in Figure 20. We can see that due to a strong defocusing, the spectrum from the Thorlabs grating presents broadened absorption lines while the amplitude hologram have sharper absorption lines. The second displays a better spectral resolution, limited by the

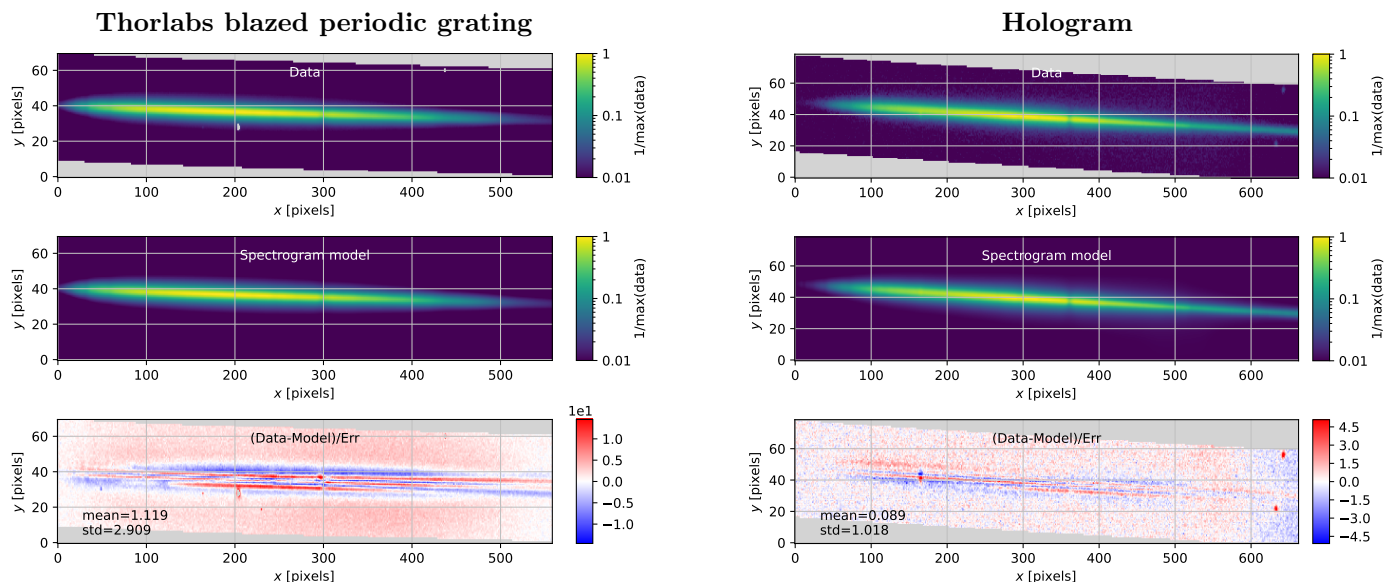


**Fig. 19.** Same as in Figure 14 but for CTIO data: HD111980 CALSPEC star observed on 2017, May 30th with a blazed Thorlabs grating 300 lines/mm (left), for which the PSF is out of focus and deviates from a Moffat model, and an amplitude hologram of 350 lines/mm (right), better focused on the CCD.

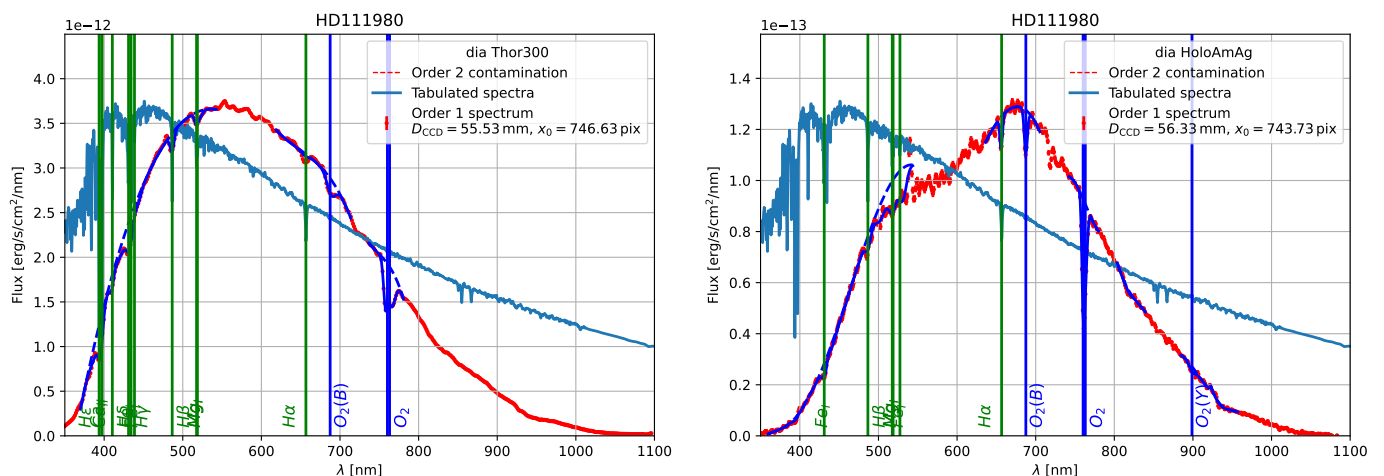


**Fig. 20.** Calibrated spectra of HD111980 CALSPEC star observed at CTIO on 2017, May 30th with a blazed Thorlabs grating 300 lines/mm (left) and an amplitude hologram of 350 lines/mm (right). The CALSPEC SEDs are given for comparison (scaled for convenience). Both dispersers do not have the same transmission curves which explains the different spectrum shapes. Vertical lines indicate emission or absorption lines that are detected, positioned at their tabulated values. Locally, the dashed blue lines show the fitted continuum and the plain blue lines are the Gaussian profiles fitted on absorption lines.

atmospheric seeing, which argues in favour of either controlling the spectrograph PSF at the hardware level, or of being able to model accurately a defocused PSF kernel. At that point, it seems easier to adjust the spectrograph to get a simple PSF model than guessing the complexity of the chromatic PSF with on-sky data. From these spectra or spectrograms, we show in Section 5 how to measure the atmospheric transmission or the instrumental transmission via a forward modelling.

## 5. A path toward atmospheric transmission measurement

One of the main objectives for us to build spectrophotometric instrument and its analysis pipeline is to be able to measure accurately on-site atmospheric transmission so as to improve the photometric calibration of other telescope on the same site. For instance, the aim of the Auxiliary Telescope at Cerro Pachón is to measure the atmospheric transmission to correct the photometry of the LSST survey.

In order to discuss the capabilities of *Spectractor* in measuring atmospheric quantities, we first recall that its main output is a first diffraction order spectrum:

$$S_1(\lambda) = T_{\text{inst},1}(\lambda) T_{\text{atm}}(\lambda | \mathbf{P}_a) S_*(\lambda). \quad (49)$$

**Table 4.** Parameters of the CTIO exposures and **Spectractor** estimations.

Parameter	CTIO Exposure 1 with blazed regular grating	CTIO Exposure 2 with amplitude hologram
Disperser	300 lines/mm	350 lines/mm
Seeing ["]	0.68	0.65
Airmass	1.12	1.13
$x_0$ [pix]	767.2	779.9
$y_0$ [pix]	696.7	702.6
$\delta y^{(\text{fit})}$ [pix]	$0.2402 \pm 0.0008$	$-0.217 \pm 0.004$
$\alpha$ [°]	$-0.7980 \pm 0.0001$	$-1.5650 \pm 0.0004$
$\langle B(\mathbf{r}) \rangle$ [ADU/s]	2.4	0.2
$D_{\text{CCD}}$ [mm]	55.53	56.33
$\mathbf{A}$ size	562	669
$r$	0.97	0.16
$N_{\text{dof}}$	125	197
Reduced $\chi^2$	9.67	1.05

To be able to get the atmospheric transmission  $T_{\text{atm}}(\lambda|\mathbf{P}_a)$ , we need to know the star SED and the instrumental transmission, and to have an accurate full forward model for the spectrograph.

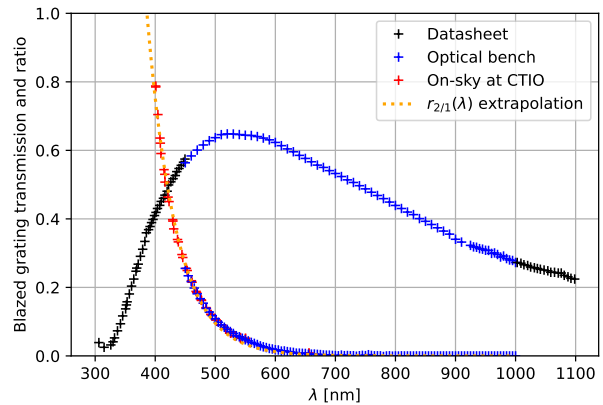
Since the most accurate PSF model is achieved with the amplitude hologram at CTIO thanks to its focusing properties, we expect better results from its analysis than from the data acquired with the Thorlabs grating.

In order to inform our forward model, we need to know both dispersers on-sky first order transmission and their  $r_{2/1}(\lambda)$  ratio. While we will show how to use on sky data to that end, we also managed to secure the Thorlabs grating to bring it back on an optical bench at the Laboratoire de Physique Nucléaire et de Hautes Énergies (LPNHE) and measure its transmission. This was not possible for the prototype hologram used at CTIO and we had to recover its transmission with on-sky data.

While in theory the forward modelling of the atmospheric transmission could be based on a perfect a priori knowledge of the instrument, and simply needs to fit each star exposure, in practice things tend to be a bit more complex. That's why we decided to show how our pipeline could be used with intermediary steps in order to gain more and more understanding of the data, up to the point where the full forward modelling of the atmospheric parameters becomes possible. Note that due to the limited telescope time and observations, this first paper relies on a limited amount of data, and aims at presenting the algorithms and procedures, being well understood that for accurate results, much more data would be needed.

The different steps that we undertook and that will be detailed are as follows:

- 5.1 laboratory measurement of the blazed grating transmission as a function of  $\lambda$ ;
- 5.2.1 inference of the CTIO 0.9 m telescope transmission using data taken with the blazed grating during a stable night;
- 5.2.2 with the CTIO 0.9 m telescope transmission, inference of the amplitude hologram transmission during the same stable night;
- 5.2.3, 5.3 with  $T_{\text{inst},1}(\lambda)$ ,  $S_*(\lambda)$ , and a Moffat PSF kernel, measurement of  $T_{\text{atm}}(\lambda|\mathbf{P}_a)$  with data using the amplitude hologram.


**Fig. 21.** First diffraction order transmission of the blazed Thorlabs grating 300 lines/mm (blue and black) and the ratio of transmissions of the order 2 over the order 1 (red, blue and orange).

### 5.1. Disperser transmission measurement

Our blazed Thorlabs 300 lines/mm grating was studied two years after the CTIO campaign on the LPNHE optical test bench. The optical bench description can be summarised as simulating a  $f/D = 18$  telescope beam of known amplitude with parabolic off-axis mirrors. A monochromator is used to select a narrow accurately known wavelength interval, and the light, after passing through the grating mounted on an  $xyz$  support, is collected on a CCD device.

The transmissions for order 0, 1 and 2 were measured using aperture photometry at many wavelengths. Unfortunately since the laboratory bench had been designed to measure filter transmissions, it couldn't be adjusted to allow for high enough signal to noise in the regions below 450 nm and above 1000 nm. For these wavelength ranges we thus resort to using the grating manufacturer spreadsheet.

Concerning the measurement of the  $r_{2/1}(\lambda)$  ratio, we use the optical bench measurement above 450 nm and the CTIO on-sky measurement from Moniez et al. (2021) below.

In order to measure wavelengths bluer than  $< 400$  nm, we extrapolate the  $r_{2/1}(\lambda)$  function with an exponential model  $C \exp[-(\lambda - \lambda_0)/\tau]$  with three free parameters  $C$ ,  $\lambda_0$  and  $\tau$  fitted on the lab data.

The first order efficiency curve and the  $r_{2/1}(\lambda)$  curve for the blazed Thorlabs 300 lines/mm grating are represented on Figure 21 and are used in **Spectractor** when measuring spectra taken with this grating (like in Figure 19 left).

### 5.2. Analysis of a photometric night

To measure the CTIO 0.9 m telescope transmission, we made use of a set of spectra acquired at different airmasses during a night with stable photometric condition. The multiplicity of the airmass conditions and the hypothesis that the atmospheric transmission spectrum only varies with the quantity of atmosphere between the source and the observer allow us to factorize the atmospheric transmission as an airmass-dependent term and the instrumental transmission term.

In order to disentangle between the average spectrum of the atmospheric transmission and the instrumental transmission spectrum we performed the fit over the  $N_s$  spectra available by simulating the atmospheric transmission with Libradtran<sup>13</sup> (Mayer & Kylling 2005; Emde et al. 2016) jointly with  $N_i$  arbitrary coefficients to sample the  $T_{\text{inst},1}(\lambda)$  curve.

At CTIO on 2017, May 30th, the night presented very stable conditions according to the *in situ* meteorological measurements of temperature, pressure, humidity, and also a stable seeing around 0.8". We analysed the spectra of CALSPEC star HD111980 acquired with the Thorlabs and holographic dispersers, under the hypothesis that this night was photometric. The observations cover an airmass range from 1 to 2 (see Figure 22).

For each one of the dispersers,  $N_s$  spectra were acquired and extracted. They were averaged in 3 nm bins, for which the instrumental transmission is supposed to be very smooth at this scale. The main atmospheric and hydrogen absorption lines have been masked in this process.

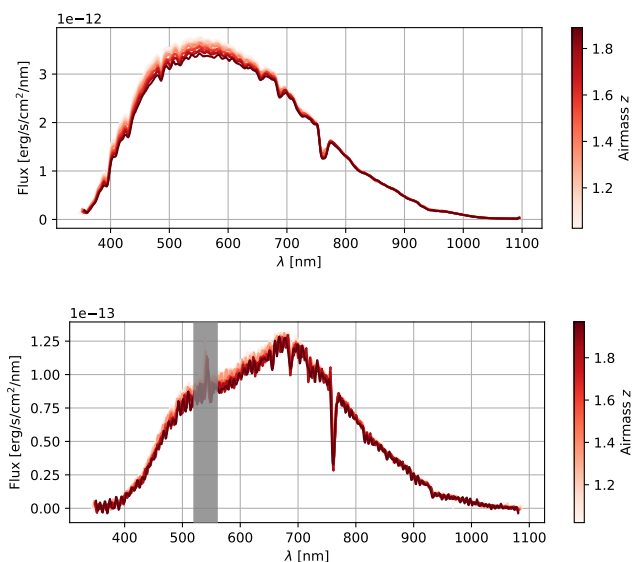


**Fig. 22.** Spectra from CALSPEC star HD111980 acquired during the assumed photometric night of 2017, May 30th at CTIO with the blazed Thorlabs grating 300 lines/mm (top) and an amplitude hologram 350 lines/mm (bottom). The curves are coloured according to the acquisition airmass  $z$ . For the amplitude hologram, a field star creates a spike around 530 nm.

### 5.2.1. Analysis of a photometric night to extract the instrumental transmission

Since the only *a priori* partial information we have in hand about the telescope transmission is the laboratory measurement of the Thorlabs grating, we start by fitting a telescope transmission model and one atmospheric model on the collection of spectra extracted from the data collected with this disperser.

From 300 nm to 1100 nm we fit simultaneously the  $N_s = 20$  good blazed grating spectra observed with the model

from equation (9) for  $p = 1$ ,

$$S_1(\lambda) = T_{\text{inst},1}(\lambda) T_{\text{atm}}(\lambda | \mathbf{P}_a) S_*(\lambda), \quad (50)$$

$S_*(\lambda)$  being the binned CALSPEC star SED, and  $T_{\text{inst},1}(\lambda)$  a vector of  $N_i = 250$  free linear amplitude parameters.

The Libradtran atmospheric transmission simulation  $T_{\text{atm}}(\lambda)$  uses the *in situ* pressure, temperature and airmass given in each exposure meta-data. In addition 3 common parameters  $P_a$  are fitted:

- the Precipitable Water Vapour (PWV, in mm);
- the ozone quantity (in dobson db);
- the Vertical Aerosols Optical Depth (VAOD).

In order to account for a possible small grey variation of the atmospheric transmission, each spectrum is weighted by a grey factor  $A_1^{(n)}$ , with their average constrained to one:

$$\langle A_1^{(n)} \rangle_n = 1 \quad (51)$$

The  $\chi^2$  we need to minimize thus writes:

$$\chi^2 = \sum_{n=1}^{N_s} \left[ \mathbf{D}_n - A_1^{(n)} S_1(\lambda) \right]^T \mathbf{C}_n^{-1} \left[ \mathbf{D}_n - A_1^{(n)} S_1(\lambda) \right] \quad (52)$$

where  $\mathbf{D}_n$  is the data vector for spectrum number  $n$  and  $\mathbf{C}_n$  its covariance matrix estimated by the Spectractor extraction pipeline. The  $A_1^{(n)}$  and  $P_a$  parameters are fitted jointly via a Gauss-Newton descent and come with their covariance matrix, while the  $T_{\text{inst},1}(\lambda)$  linear parameters are computed analytically via the usual algebra at each descent step. Since the spectrum of the star is supposed known, no regularisation is needed. As the instrumental transmission is assumed to be smooth, the descent is repeated with a  $5\sigma$  clipping to remove outliers.

This procedure has been tested on simulations, and we checked that it recovered the injected parameters for instrumental transmission, grey factors and atmospheric quantities within the uncertainty ranges.

The results obtained on the CTIO data are presented in Figure 23. Approximately 15% of the 5000 spectral data points end up masked, either because they are close to a spectral line or because they are  $5\sigma$  outliers. Residuals are structured below the  $2\sigma$  level in the red part of the spectra, either because of an incorrect PSF model for the redder wavelengths due to defocusing or because of PWV variations in the atmosphere, as hinted by the spectra, vertically ordered in time.

The best  $T_{\text{inst},1}(\lambda)$  solution that we managed to extract is presented in Figure 24. The black points represent the raw fitted  $T_{\text{inst},1}(\lambda)$  vector, and the red curve is smoothed with a Savitzky-Golay filter of order 1 and window size 17. Error bars result from the combination of raw uncertainties from the fit plus the difference between the smoothed curve and the scattered raw black points. This leads to larger uncertainties for the instrumental throughput where the spectra were masked, around the main absorption lines.

The transmission curve presents the expected decreases due to the loss of efficiency of the CCD. Given the measurement of the blazed Thorlabs grating at the lab (Figure 21), we extracted the CTIO 0.9 m instrumental throughput from the  $T_{\text{inst},1}(\lambda)$  smoothed curve.

<sup>13</sup> <http://www.libradtran.org>

This fills the lack in *a priori* knowledge of the telescope throughput to inform our forward model, and will be used in the following analysis. We obtain the telescope throughput by dividing the fitted instrumental transmission by the first order efficiency of the blazed Thorlabs grating. The atmospheric transmission results are detailed in Section 5.2.3.

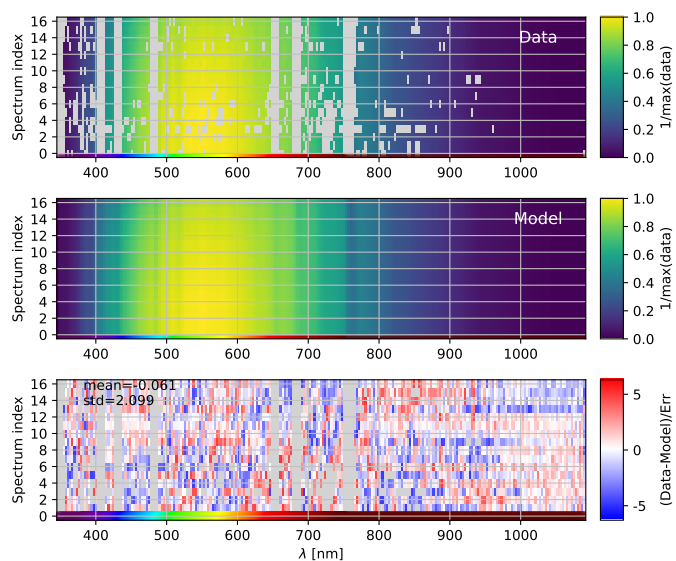


**Fig. 23.** Multispectra fit of a CTIO photometric night using the blazed grating 300 lines/mm. *Top*: the  $D_n$  data spectra binned in 3 nm intervals, indexed vertically by their index  $n$  and with a coloured amplitude. The grey colour stands for masked regions. *Middle*: the best fitting spectrum models  $A_1^{(n)}S_1(\lambda)$  indexed vertically by their index  $n$ . *Bottom*: map of the residuals.

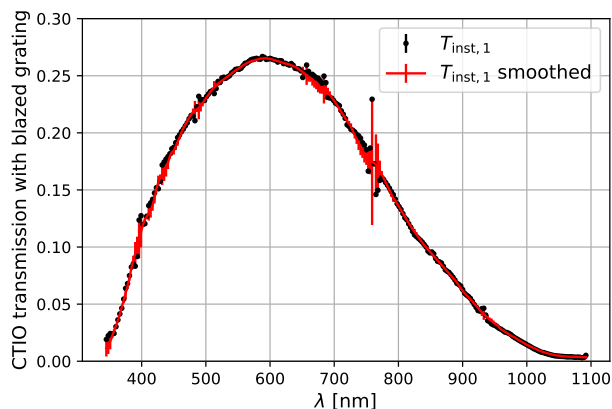


**Fig. 24.** Measured  $T_{\text{inst},1}(\lambda)$  curve for the CTIO 0.9 m telescope equipped with a Thorlabs 300 lines/mm blazed grating (black points) from a photometric night. The red curve is a smoothing using a Savitzky–Golay filter of order 1 and window size 17.

A more accurate estimate of the instrumental transmission would need more data both to inform a better PSF model, and to constrain more closely the atmospheric transmission variations. Given the limited amount of data available, our goal was to illustrate how a forward model approach can be adjusted to gain more information on the different components of the model.

We find it also noteworthy that the procedure is symmetric with respect to atmospheric transmission and telescope transmission: the need for the Libradtran model as *a priori* to constrain the atmospheric transmission shape could be replaced by the *a priori* measurement of the telescope transmission.

## 5.2.2. Analysis of a photometric night to get amplitude hologram transmissions

The next step needed to inform further our forward model in order to use the best quality data to constrain the atmospheric transmission is to estimate the holographic disperser transmission. If this transmission is known, it becomes possible to use the data gathered with this disperser and take advantage of the fact that its PSF can be fairly well modelled with a Moffat.

In order to obtain the hologram transmission we use the same procedure than described for the Thorlabs disperser above on data collected during the same photometric night but with the holographic disperser. However the ratio  $r_{2/1}(\lambda)$  is still a prior information needed for the full forward model. For the holographic disperser, we built  $r_{2/1}(\lambda)$  using only the interpolated on-sky data presented in Moniez et al. (2021) Figure 21.

The  $N_s = 27$  spectra are presented in Figure 22 and the results are presented in Figure 25. Approximately 0.5% of the 6723 data points end up masked. Residuals are below  $3\sigma$ . A deep absorption feature is visible around the water absorption band at 950 nm.

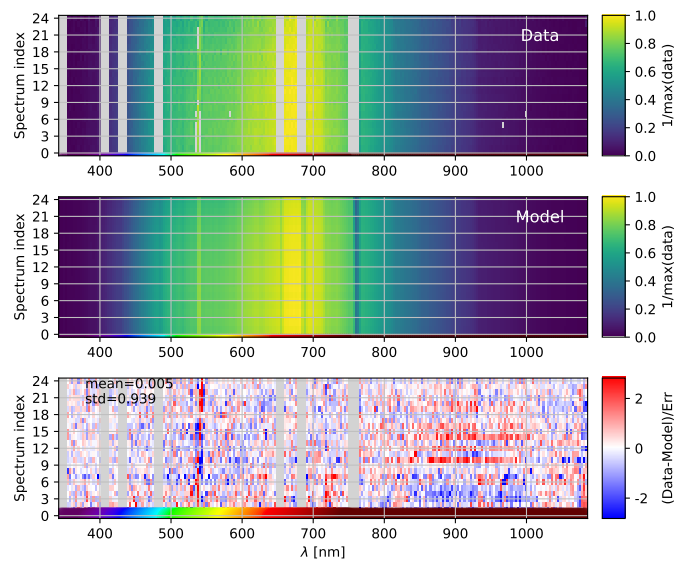


**Fig. 25.** Multispectra fit of a CTIO photometric night using the amplitude hologram 350 lines/mm. *Top*: the  $D_n$  data spectra binned in 3 nm intervals, indexed vertically by their index  $n$  and with a coloured amplitude. The grey colour stands for masked regions. *Middle*: the best fitting spectrum models  $A_1^{(n)}S_1(\lambda)$  indexed vertically by their index  $n$ . *Bottom*: map of the residuals.

As in the previous section, from the  $T_{\text{inst},1}(\lambda)$  best fit (see Figure 26) we deduced the transmission of the first diffraction order for the holographic disperser, using the CTIO 0.9 m telescope transmission curve determined previously. We are well aware of the systematic errors present

in these results, and stress that they are presented here to illustrate how the forward model approach we implemented can be used when lacking *a priori* information on crucial components of the model.

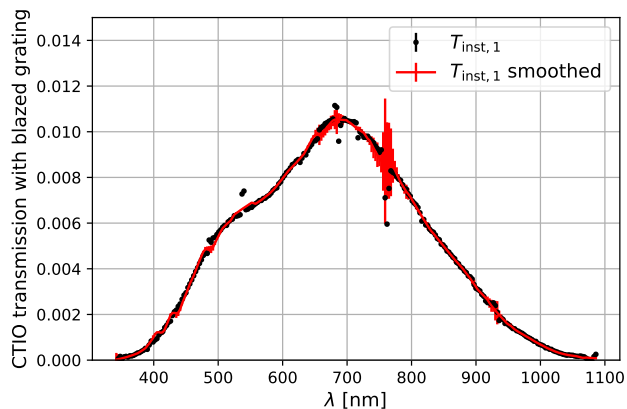


**Fig. 26.** Measured  $T_{\text{inst},1}(\lambda)$  curve for the CTIO 0.9 m telescope equipped with an amplitude holographic grating of around 350 lines/mm (black points) from a photometric night. The red curve is a smoothing using a Savitzky–Golay filter of order 1 and window size 11.

### 5.2.3. Analysis of a photometric night to extract atmospheric parameters

In addition to the instrumental transmissions of both dispersers, the procedures above also yield the parameters describing the mean atmospheric transmission of the night. These results, under the assumption that the night was photometric, are presented in Table 5.

**Table 5.** Atmospheric parameters  $P_a$  fitted for the same photometric night of 2017, May 30th, observing CALSPEC star HD111980 with two different dispersers. Last line gives the MERRA-2 value measured in a 60 km wide cell around CTIO.

Disperser	aerosols VAOD	ozone db	PWV mm	$\chi_{\text{red}}^2$
Thorlabs	$0.020 \pm 0.001$	$314 \pm 2$	$2.00 \pm 0.04$	8.3
Ampl. holo.	$0.016 \pm 0.003$	$284 \pm 9$	$2.2 \pm 0.1$	2.4
MERRA-2	0.017	265	4 – 5	

The rather low value of the reduced  $\chi^2$  for the amplitude hologram illustrates the focussing properties of this disperser, that allow us to describe its PSF quite accurately with a simple 2D Moffat. Quantities obtained from the blazed Thorlabs grating data show lower statistical uncertainties than amplitude hologram data as their signal-to-noise ratio is much higher (because of its much higher transmission). However they certainly suffer from higher

unevaluated PSF systematics than the hologram measurements. The difference between the two estimates of the atmospheric transmission in Table 5 leads to variations in synthesized broadband magnitudes for the LSST filters of about 8 mmag in u, g and r filters, 3 mmag in i, 1.5 mmag in z and 4 mmag in y filter, for various standard CALSPEC SEDs and supernovae at redshift 0. The milli-magnitude accuracy on atmospheric transmission can thus be reached provided that the atmospheric parameters accuracy reaches below the difference shown in Table 5: we found that PWV must be fitted with an accuracy better than  $\approx 0.05$  mm to get milli-magnitude accuracy in y band. For VAOD, uncertainties of about 0.001 are required for u, g and r bands. For ozone, 10 db precision is enough to get milli-magnitude in r band.

We find also interesting to note that the ozone and VAOD parameters we fitted are similar to what the global meteorological network MERRA-2<sup>14</sup> (Gelaro et al. 2017) estimates for the CTIO site during that night. The MERRA-2 PWV value ranges from 4 to 5 mm during the 2017 May 30th night. As MERRA-2 averages atmospheric quantities in 60 km wide cells, it can be expected that quantities with large local variations like water vapour could differ from on-site measurements. This is even more true for CTIO, located at the top of a Chile mountain. On the other hand, a high-atmospheric quantity would be expected to depart less between on-site and satellite measurements. We report MERRA-2 values and compare to what we extract with our forward model to illustrate how, given a detailed knowledge of the telescope, one can tackle the challenging problem of on site atmospheric transmission measurement. While the error bars quoted only propagate statistical uncertainties, and are probably dominated by systematics, the tentative concordance between the parameters measured by MERRA-2 and our forward model results support the algorithm developed.

For completeness, we also present for the holographic disperser data, the evolution of the grey parameters  $A_1^{(n)}$  through the night in Figure 27 together with the final correlation matrix of the fitted parameters in Figure 28. The 27  $A_1^{(n)}$  factors variation is less than 1%. This supports the first order approximation of the night as being photometric and shows again the ability of the procedure to improve our understanding of the data, offering venues to improve the model.

Finally, we note that the correlation matrix exhibits that the VAOD aerosol parameter is particularly correlated to the spectrum amplitudes. This doesn't come as a surprise since this quantity is mostly determined by the spectrum slope for  $\lambda \approx 400$  nm. So any systematic on the amplitude of the spectrum affects directly the estimate of aerosols.

### 5.3. Atmospheric forward model approach

After illustrating how the forward model approach could be used to measure the telescope and disperser transmissions, yielding a set of stellar and atmospheric transmission spectra, we can go one step further. Assuming that our measurement of those crucial components of the forward model had been done with enough data to be accurate, it becomes possible to skip the spectrum extraction part and directly fit the atmospheric parameters on the raw spectrogram.

<sup>14</sup> <https://gmao.gsfc.nasa.gov/reanalysis/MERRA-2/>

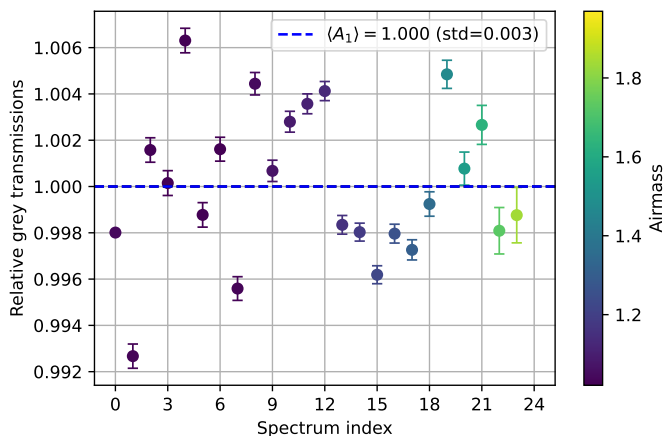


**Fig. 27.** Measured  $A_1^{(n)}$  grey absorption factors for the CTIO 2017, May 30th night, observing CALSPEC star HD111980, for each spectra (ordered in time).

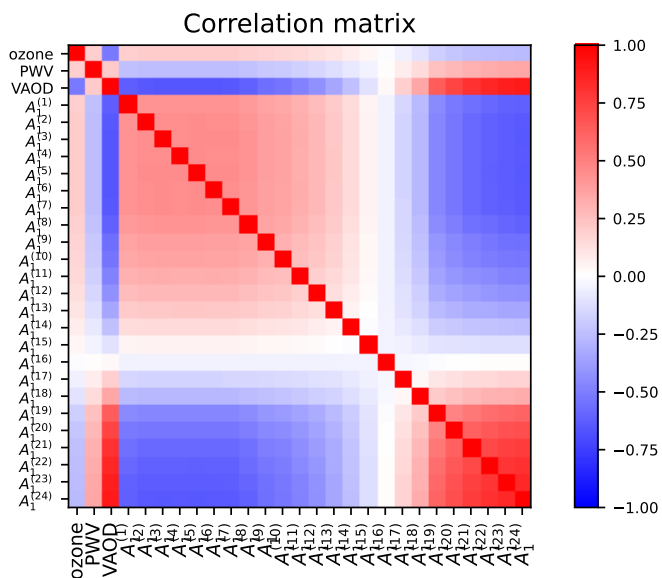


**Fig. 28.** Correlation matrix for the multispectra parameters fitted for the CTIO 2017, May 30th night, observing CALSPEC star HD111980.

At the cost of having access to the transmissions aforementioned, if we model the spectrum  $S_1(\lambda)$  as the product of a known instrumental transmission  $T_{\text{inst},1}(\lambda)$ , a Libradtran atmospheric model  $T_{\text{atm}}(\lambda|\mathbf{P}_a)$  and a known CALSPEC star SED  $S_*(\lambda)$ , we can describe any observed spectrogram as:

$$\mathbf{I}(\mathbf{Z}|\mathbf{A}, \mathbf{r}_c, \mathbf{P}) = \tilde{\mathbf{M}}(\mathbf{Z}|\mathbf{r}_c, \mathbf{P}) \mathbf{A} \quad (53)$$

$$\mathbf{A}(\lambda) = A_1 T_{\text{inst},1}(\lambda) T_{\text{atm}}(\lambda|\mathbf{P}_a) S_*(\lambda) \quad (54)$$

with  $A_1$  a grey factor.

As before, the parameters and their covariance matrix are estimated via a Gauss-Newton descent minimizing a  $\chi^2$  calculated over a single spectrogram. The parameters fitted are  $A_1, A_2, \delta y^{(\text{fit})}, P_a, D_{\text{CCD}}, \alpha$  and all the polynomial coefficients modelling the wavelength dependence of the PSF kernel. Each spectrogram is fitted independently. We call

this a *spectrogram fit*. As a comparison, and a way to assess the quality of the stellar spectra forward model, we also fit  $S_1(\lambda)$  and the atmospheric transmission directly on the stellar spectra extracted at that step. We call this a *spectrum fit*.

### 5.3.1. Qualification on simulations

The atmospheric parameter extraction directly from a spectrogram has been tested on simulations. The chosen parameters to simulate them were the extracted parameters found from fitting all data spectrograms of the "photometric" night of 2017, May 30th involving the amplitude hologram. With those parameters we simulated spectrograms of a CALPSEC star spanning airmass  $\approx 1$  to  $\approx 2$  with the same seeing and atmospheric conditions than that of our data. We fixed arbitrarily the unknown  $P_a$  parameters to 300 db for ozone, 0.03 for VAOD and 5 mm for PWV.

The result of the *spectrogram fit* is very similar to what was presented in Figure 10. For comparison we present the result of the *spectrum fit* of the extracted spectrum from one of the simulated spectrograms in Figure 29. We see that the extracted spectrum (red points), the best fitting spectrum model (blue) and the true spectrum (green) are all in agreement within the quoted uncertainties.

In addition, the recovered atmospheric values are compatible with the true injected values within uncertainties, with a strong correlation between the grey parameter  $A_1$  and the aerosols, as seen before on real data. The nightly behaviour is presented in Figure 30. All values agree with the true values for both methods, correctly accounting for the variable simulated conditions.

We note again a strong correlation between the VAOD and the  $A_1$  parameter. As mentioned before, this is an expected behaviour as aerosols specifically affect spectrum slope in the blue and the global spectrum amplitude.

In addition to validating the spectrogram fit, these results also show that the forward model process and all the pipeline steps presented above do not bias the measurement of the atmospheric parameters.

### 5.3.2. Data analysis

The individual fits of the spectrograms and spectra extracted from CTIO data are presented in Figures 31, 32 and 33.

We see that the atmospheric forward modelling fits the data at the  $5\sigma$  uncertainty level but that the PSF model imprints structured residuals similarly to what happens in the full forward model case (Figure 19). This effect is visible along the spectrogram and inside the dioxygen absorption line.

The spectrum presented in Figure 32 is globally well fitted by the  $S_1(\lambda)$  model. The fit residuals around the main dioxygen line for data as well for simulation are compatible with the instrumental throughput uncertainties. All spectrograms and spectra of the night show the same residual patterns. Concerning the atmospheric parameters we see that both methods yield very similar values. The *spectrogram fit* values are smooth in time, with a visible correlation between VAOD and  $A_1$  parameters, while the *spectrum fit* values are shifted and more scattered probably due to the

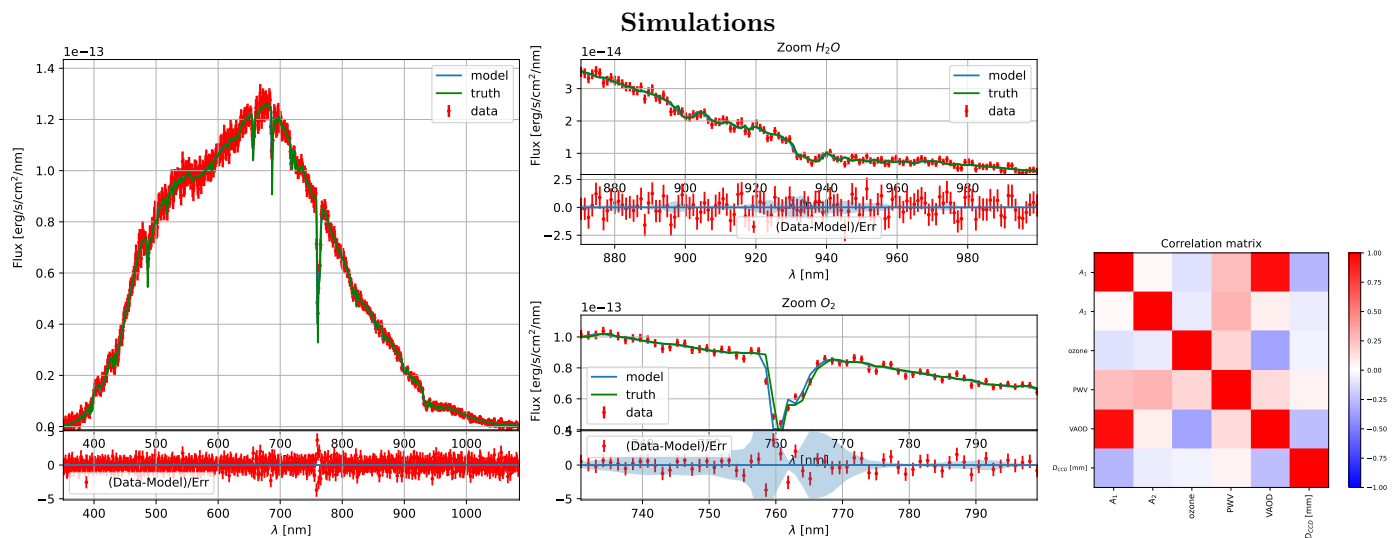


**Fig. 29.** Results from the  $S_1(\lambda)$  model fit on HD111980 CALSPEC star spectrum, extracted from a simulated spectrogram. *Left:* spectrum data (red) compared with the best fitting model (blue) and the model uncertainties (light blue band) due to the CTIO telescope transmission uncertainties, the true injected spectrum in the simulation (green), and the residuals (bottom). *Middle:* zoom around the dioxygen line at 762 nm and zoom on the  $H_2O$  absorption band around 950 nm. *Right:* Correlation matrix of the fitted parameters.

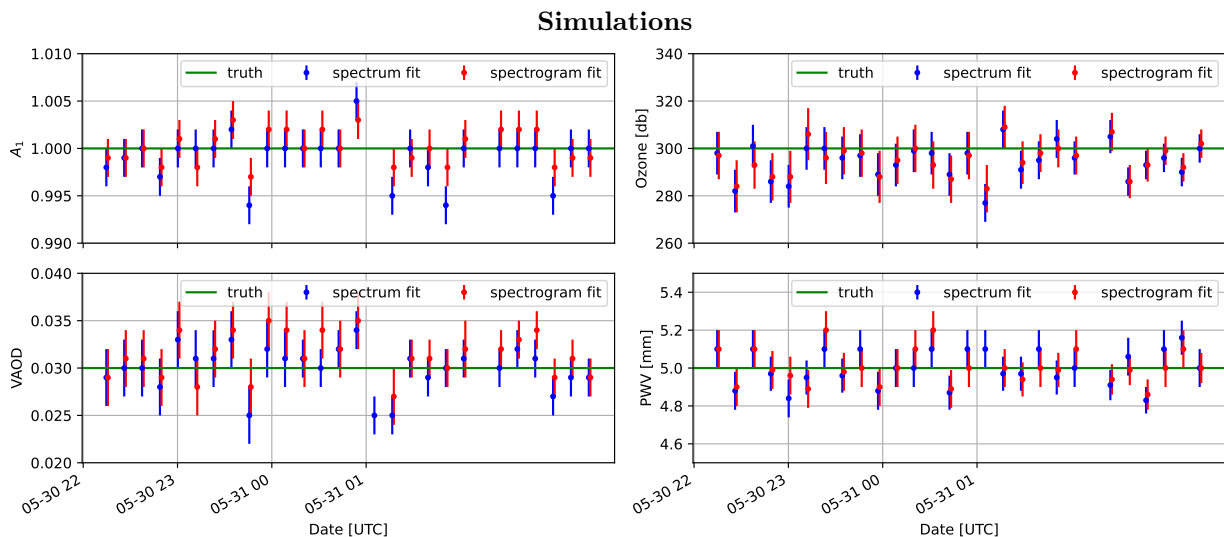


**Fig. 30.** Evolution of the atmospheric parameters along the simulation of the 2017 May 30th night, observing CALSPEC star HD111980 with an amplitude hologram. The blue points comes from the spectrum fits, while the orange points are from the spectrogram fits. The green line gives the true values injected in the simulations.

higher sensitiveness of this simpler procedure to outliers like the field star contamination of the spectra around 530 nm.

We remind here that in the *spectrogram fit* the raw spectrogram data are directly fitted with a model that contains the instrumental transmission for diffraction orders 1 and 2, a Libradtran atmospheric model, and models for the dispersion relationship and PSF kernel.

At this point, the smoothness of the atmospheric parameter curves and the reasonable values that we obtained (low ozone, a few millimetres of precipitable water vapour) are the closest to reality that we can expect to get with the quality and size of the data set at hand.

We again acknowledge that these atmospheric results are affected by systematic uncertainties and choices (like

the circularity of the PSF model, the second diffraction order PSF size or the blazed grating transmission model) that affect the absolute value of the quoted parameters. Unfortunately we have not enough data to estimate systematics and go further. We leave the careful analysis of the atmospheric transmission for a future paper, for example using the high quality data set promised by AuxTel, which is dedicated to measure atmospheric transmission at the Rubin Observatory site.

## 6. Summary and conclusions

Slitless spectrophotometry with forward modelling open a path toward the acquisition of spectra with imaging tele-

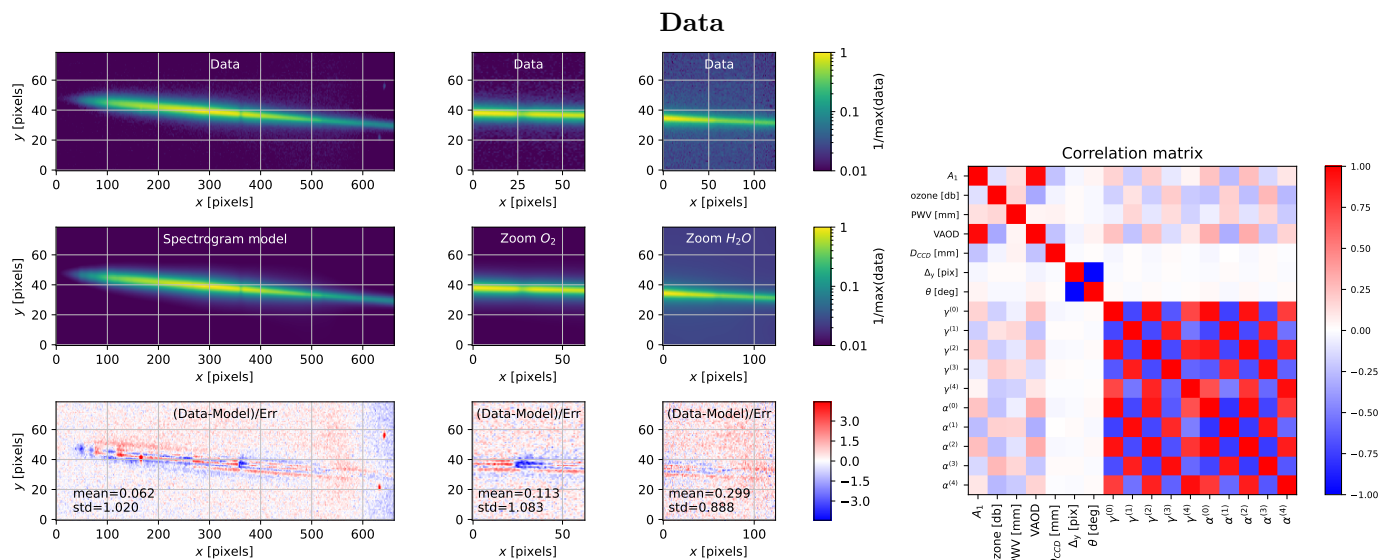


**Fig. 31.** Results from the atmospheric forward model of HD111980 CALSPEC star with a Moffat PSF kernel (shape parameters evolve as a polynomial function of order 4), observed with an amplitude hologram of 350 lines/mm. *Left:* spectrogram data (top), best fitting spectrogram model (middle) and residuals in units of  $\sigma$  (bottom) *Middle:* zoom around the dioxygen line at 762 nm and zoom on the  $H_2O$  absorption band around 950 nm. All color maps are normalised by the maximum of the simulated spectrogram. *Right:* Correlation matrix of the fitted parameters.

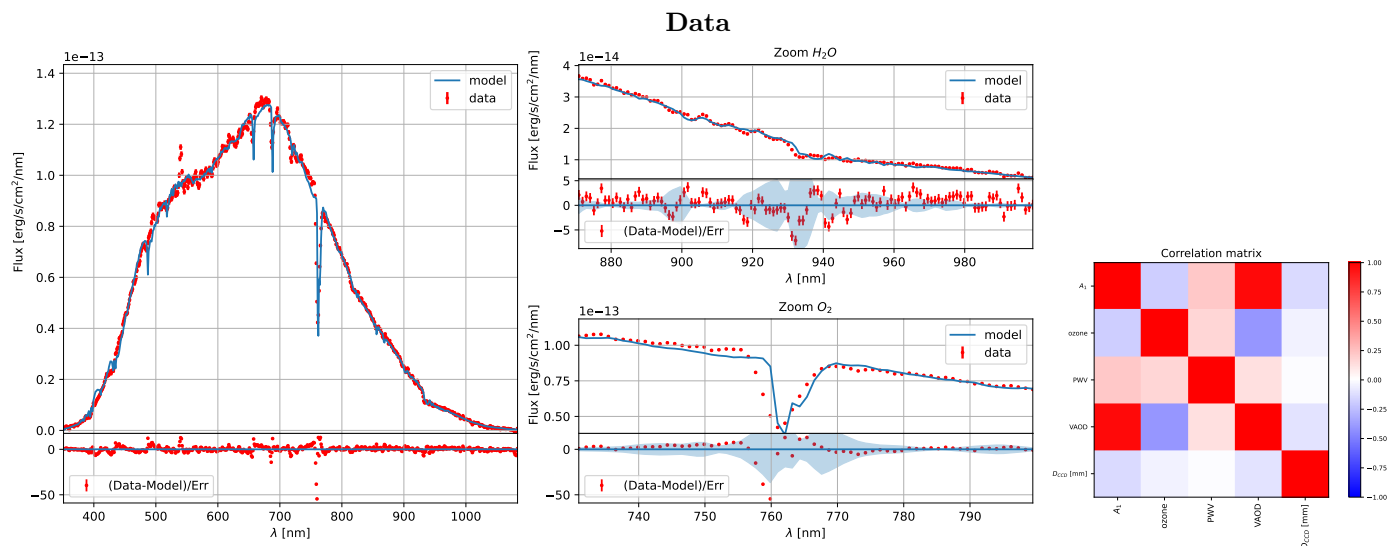


**Fig. 32.** Results from the  $S_1(\lambda)$  model fit on HD111980 CALSPEC star spectrum. *Left:* spectrum data (red) compared with the best fitting model (blue, mostly behind the green curve) and the model uncertainties (light blue band) due to the CTIO telescope transmission uncertainties, and the residuals (bottom). *Middle:* zoom on the dioxygen line at 762 nm and zoom on the  $H_2O$  absorption band around 950 nm. *Right:* Correlation matrix of the fitted parameters.

scopes simply transformed into spectrographs by inserting a disperser on the light path.

We demonstrated on simulations that building a forward model of a spectrogram allows for accurate spectrophotometry, with a spectral resolution that only depends on the PSF width along the dispersion axis. The key of the process is a regularisation algorithm, fed with as much as prior information as possible (regularity of the searched spectrum, PSF parametrisation, ADR, grating efficiency). The two key functions of the model are the dispersion function  $\Delta_p(\lambda)$  and the PSF model  $\phi(\mathbf{r}, \lambda)$ , plus the knowledge of the  $r_{p/1}(\lambda)$  ratio of diffraction order transmissions.

We exemplified how this procedure functions on real data, with tentatively very promising results. Being aware of the limits of the data set in our possession, we took great care to exemplify how the forward model procedure can be used to improve our knowledge of the data, and by doing so, to inform the forward model.

We can also summarize some of the important lessons learned while implementing the *Spectractor* pipeline as follows.

- Forward modelling provides a modular approach where each brick is a physical or empirical model that can be changed or improved depending on the data particular-

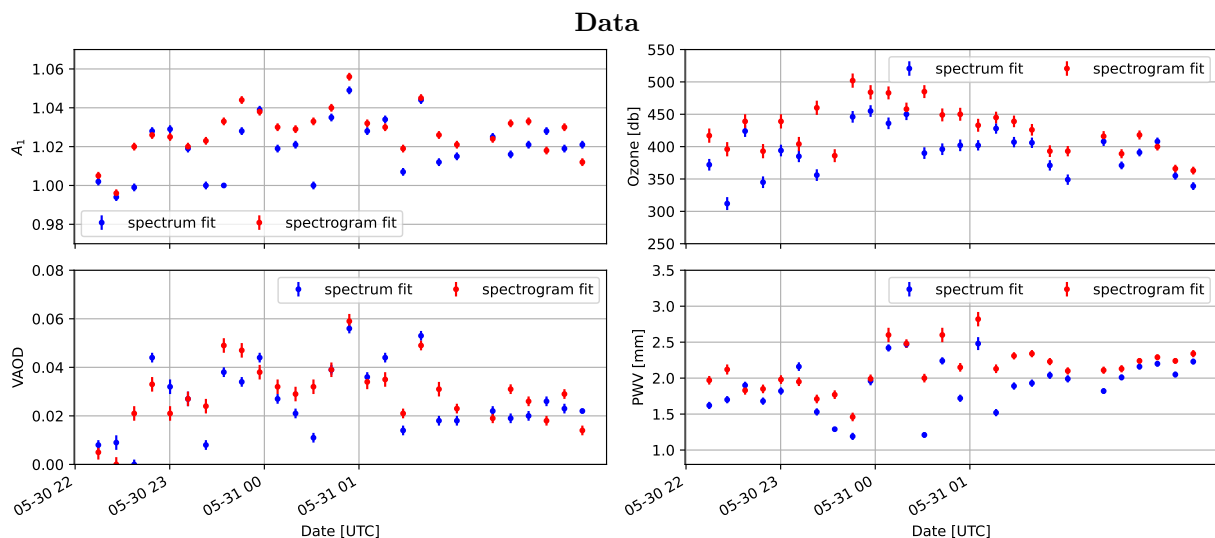


**Fig. 33.** Evolution of the atmospheric parameters as a function of the exposure time during the 2017 May 30th night, observing CALSPEC star HD111980 with an amplitude hologram. The blue points comes from the spectrum fits, while the orange points are from the spectrogram fits.

ities and signal to noise ratio. Residuals indicate how to improve the model (data rules).

- Once implemented, forward modelling easily provides the capability to simulate data sets to test new algorithms.
- Second diffraction order is not a contamination but a signal that helps recovering the blue part of the order 1 spectrum. It should be taken advantage of whenever possible. This in particular needs to rethink the common wisdom of spectroscopy by increasing the efficiency of the grating in the second order, and use a field rotator (if available) in order to more easily separate the different diffraction orders on the sensor thanks to ADR.
- The accurate knowledge of the PSF is thus crucial and requires dedicated data and analysis that need to be carefully budgeted for. The PSF width sets the spectral resolution and the number of degrees of freedom that can be extracted from data, thus decreasing the width is crucial.

Since the main scientific driver for the development of *Spectractor* is the measurement of on-site atmospheric transmission, we pushed our analysis all the way to that point. We showed how our procedure allows us to measure the on-sky telescope transmission all the way to the direct extraction of atmospheric parameters from spectrograms.

While the atmospheric parameters are dominated by systematic uncertainties, in particular from our partial knowledge of the instrumental transmission and of the PSF, the comparison with satellite data shows a promising tentative agreement. We defer as work beyond this paper devoted to presenting the spectrophotometry method, a more intensive study of on site atmosphere transmission. This will in particular require access to much more data, and specific detailed analysis to obtain accurate instrumental transmissions and PSF model.

We finally would like to acknowledge that many elements of the forward model can, and will be improved as new data becomes available. In particular we can imagine estimating the background directly in the forward model,

including other diffraction orders, modelling the field star spectrogram contaminations, integrate the chromatic flat-fielding in the model to account for pixel efficiencies, etc.

These ideas are worth implementing in the algorithm if required by data. On the other hand, there are also many hardware solutions that can be implemented to increase the *a priori* knowledge of the instrument and improve greatly the forward model analysis. For instance we showed that holographic dispersers like those presented in Moniez et al. (2021) improve the focusing of the spectrogram on the sensor on the whole visible and near infra-red range which eases the modelling of the PSF. Also, its narrow width allows better spectral resolution. Another improvement would be using a Collimated Beam Projector (Coughlin et al. 2016; Souverin et al. 2022) to measure the telescope transmission at the permil level, and monitor its evolution with time.

In conclusion, we have presented in this paper the theoretical tools, together with a detailed implementation example to add spectro-photometric ability to an imager by the insertion of a disperser on the light path. This comes at some computational cost, readily available nowadays, but also requires either *a priori* knowledge of the instrument or dedicated data and analysis to bring the model to the required level of accuracy.

As closing remark, we would like to stress that the forward model approach is extremely powerful, but requires a deep focus on analysing the data in hands, and solving the problems that are present. We found many times that trying to put together a generic forward model that suits all needs is a fools quest, and realised again and again that implementation choices matter.

*Acknowledgements.* We are grateful to the CTIO technical staff members Hernan Tirado and Manuel Hernandez for their help during our tests with the CTIO 0.9 m telescope. We also thank Mélanie Cheavance for her participation to the observations and Augustin Guyonnet for fruitful advice for the CTIO image reduction. The cost of the observations have been shared by the IJCLab (IN2P3-CNRS) and the Department of Physics and Harvard-Smithsonian Center for Astrophysics, Harvard University. F.B. is part of the FP2M federation (CNRS FR 2036) and of the project Labex MME-DII (ANR11-LBX-0023-01). This paper has undergone internal review in the LSST Dark En- ergy

Science Collaboration. The internal reviewers were Marc Betoule, Andres Plazas-Malagon and David Rubin.

J. Neveu is the primary author of the paper and of the Spectractor software, leading the analysis toward measurement of atmosphere transmission measurement. V. Brémaud implemented the atmospheric differential refraction in the forward model, and wrote the pipeline to determine the CTIO telescope throughput. F. Barret brought the mathematical frame for the regularisation procedure. S. Bongard contributed with general discussions on the spectrum extraction and atmospheric physics. Y. Copin developed the theoretical framework of slitless spectrophotometry and of the forward modelling. S. Dagoret-Campagne and M. Moniez contributed with general discussions on spectrum extraction, the data taking and analysis of CTIO data. L. Le Guillou built the specific system to measure the disperser transmission on the LPNHE optical bench and measured the dispersers. P. Antilogus, C. Juramy and E. Sepulveda built and maintained the LPNHE optical bench. The DESC acknowledges ongoing support from the Institut National de Physique Nucléaire et de Physique des Particules in France; the Science & Technology Facilities Council in the United Kingdom; and the Department of Energy, the National Science Foundation, and the LSST Corporation in the United States. DESC uses resources of the IN2P3 Computing Center (CC-IN2P3-Lyon/Villeurbanne - France) funded by the Centre National de la Recherche Scientifique; the National Energy Research Scientific Computing Center, a DOE Office of Science User Facility supported by the Office of Science of the U.S. Department of Energy under Contract No. DE-AC02-05CH11231; STFC DiRAC HPC Facilities, funded by UK BEIS National E-infrastructure capital grants; and the UK particle physics grid, supported by the GridPP Collaboration. This work was performed in part under DOE Contract DE-AC02-76SF00515.

Mayer, B. & Kylling, A. 2005, *Atmospheric Chemistry and Physics*, 5, 1855  
 Moniez, M., Neveu, J., Dagoret-Campagne, S., et al. 2021, *Monthly Notices of the Royal Astronomical Society*, 506, 5589  
 Murty, M. V. R. K. 1962, *J. Opt. Soc. Am.*, 52, 768  
 Neveu, J., Brémaud, V., Dagoret-Campagne, S., & Fisher-Levine Merlin. 2021, Spectractor: Spectrum extraction tool for slitless spectrophotometry  
 Outini, M. & Copin, Y. 2020, *A&A*, 633, A43  
 Perlmutter, S., Aldering, G., Goldhaber, G., et al. 1999, *The Astrophysical Journal*, 517, 565  
 Riess, A. G., Filippenko, A. V., Challis, P., et al. 1998, *The Astrophysical Journal*, 116, 1009  
 Robertson, J. G. 1986, *PASP*, 98, 1220  
 Rubin, D., Aldering, G., Antilogus, P., et al. 2022, Uniform Recalibration of Common Spectrophotometry Standard Stars onto the CALSPEC System using the SuperNova Integral Field Spectrograph  
 Ryan, R. E., Casertano, S., & Pirzkal, N. 2018, *Publications of the Astronomical Society of the Pacific*, 130, 034501  
 Schroeder, D. & Inc, E. I. 2000, *Astronomical Optics, Electronics & Electrical* (Elsevier Science)  
 Scolnic, D. M., Jones, D. O., Rest, A., et al. 2018, *The Astrophysical Journal*, 859, 101  
 Souverin, T., Neveu, J., Betoule, M., et al. 2022, Measurement of telescope transmission using a Collimated Beam Projector  
 The Nearby Supernova Factory, Buton, C., Copin, Y., et al. 2013, *A&A*, 549, A8  
 Wahba, G. 1990, *Spline Models for Observational Data*, CBMS-NSF Regional Conference Series in Applied Mathematics (Society for Industrial and Applied Mathematics (SIAM, 3600 Market Street, Floor 6, Philadelphia, PA 19104))

## References

Ade, P. A. R., Aghanim, N., Arnaud, M., et al. 2016, *Astronomy & Astrophysics*, 586, A141  
 Bertin, E. & Arnouts, S. 1996, *A&AS*, 117, 393  
 Betoule, M., Marriner, J., Regnault, N., et al. 2013, *Astronomy & Astrophysics*, 552, A124  
 Betoule, M., Kessler, R., Guy, J., et al. 2014, *A&A*, 568, A22  
 Betoule, Marc, Antier, Sarah, Bertin, Emmanuel, et al. 2023, *A&A*, 670, A119  
 Birch, K. P. & Downs, M. J. 1993, *Metrologia*, 30, 155  
 Birch, K. P. & Downs, M. J. 1994, *Metrologia*, 31, 315  
 Bohlin, R. C., Gordon, K. D., & Tremblay, P.-E. 2014, *Publications of the Astronomical Society of the Pacific*, 126, 711  
 Bohlin, R. C., Hubeny, I., & Rauch, T. 2020, *AJ*, 160, 21  
 Bolton, A. S. & Schlegel, D. J. 2010, *PASP*, 122, 248  
 Bradley, L., Sipőcz, B., Robitaille, T., et al. 2020, *astropy/photutils*: 1.0.0  
 Burke, D. L., Axelrod, T., Blondin, S., et al. 2010, *The Astrophysical Journal*, 720, 811  
 Burke, D. L., Rykoff, E. S., Allam, S., et al. 2017, *The Astronomical Journal*, 155, 41  
 Coughlin, M., Abbott, T. M. C., Brannon, K., et al. 2016, in *Observatory Operations: Strategies, Processes, and Systems VI*, ed. A. B. Peck, R. L. Seaman, & C. R. Benn (SPIE)  
 Edlén, B. 1966, *Metrologia*, 2, 71  
 Emde, C., Buras-Schnell, R., Kylling, A., et al. 2016, *Geoscientific Model Development*, 9, 1647  
 Gelaro, R., McCarty, W., Suárez, M. J., et al. 2017, *Journal of Climate*, 30, 5419  
 Golub, G. H., Heath, M., & Wahba, G. 1979, *Technometrics*, 21, 215  
 Hall, J. T. 1966, *Appl. Opt.*, 5, 1051  
 Hansen, P. 1992, *SIAM Review*, 34, 561  
 Hansen, P. 2010, *Discrete Inverse Problems: Insight and Algorithms*, *Fundamentals of Algorithms* (Society for Industrial and Applied Mathematics)  
 Hazenberg, F. 2019, *Theses*, Sorbonne Université  
 Horne, K. 1986, *PASP*, 98, 609  
 Houston, J. M. & Rice, J. P. 2006, *Metrologia*, 43, S31  
 Ingraham, P., Clements, A. W., Ribeiro, T., et al. 2020, in *Society of Photo-Optical Instrumentation Engineers (SPIE) Conference Series*, Vol. 11452, *Society of Photo-Optical Instrumentation Engineers (SPIE) Conference Series*, 114520U  
 Lang, D., Hogg, D. W., Mierle, K., Blanton, M., & Roweis, S. 2010, *AJ*, 139, 1782  
 Li, M., Li, G., Lv, K., et al. 2019, *MNRAS*, 484, 2403

## Appendix A: Astrometry

Accurately anchoring the wavelength calibration is crucial in many regards. For atmospheric transmission measurement, a small shift of about 1 nm can bias significantly the estimate of the aerosol parameters. Unfortunately, such a shift can happen because of the poor determination of the position of the order 0 of the spectrum which is usually saturated with long bleeding spikes. Localizing it accurately is difficult and might not be robust enough to achieve a centroid determination precision better than the pixel scale for every image in every circumstances.

We thus found useful to explore how to use the field stars to set a precise astrometry using the `astrometry.net` library<sup>15</sup>.

The field stars centroids are first extracted from the image using the `IRAFStarFinder` method from `photutils` library (Bradley et al. 2020), using a  $5\sigma$  clipping above threshold.

The `astrometry.net solve-field` function is then called: patches of stars are compared to known asterisms to obtain the precise location of the image on sky as well as the transformation between image coordinates and sky coordinates in the form of a World Coordinate System (WCS) description.

This procedure may not yield sub-pixel precision for the target star centroid, in particular if it has a high proper motion. To improve the precision, we compare the first source catalogue whose positions are converted in sky coordinates, with star positions from the *Gaia* DR2 catalogue corrected from their proper motion.

The difference between the 50 brightest field star coordinates in the two catalogues is subtracted to the WCS solution in order to lock it on the *Gaia* catalogue.

We then remove the star with the largest distance to the *Gaia* catalogue, and reapply `astrometry.net` followed by the *Gaia* catalogue centering, and repeat 10 times this operation. The astrometric solution where the distance between the image stars and the *Gaia* stars is the smallest is kept. This procedure minimizes the effect of stars with bad reconstructed centroids (due to saturation effects) or high proper motions. It ends with a scatter evaluated at  $\approx 0.15''$  RMS (Figure 7).

## Appendix B: Gauss-Newton minimisation algorithm

The gradient descent to minimize a  $\chi^2$  using the Gauss-Newton algorithm works as follow. Let's consider a data set with  $N$  data points gathered into a vector  $\mathbf{D}$  with their uncertainties (correlated or not) represented by a matrix  $\mathbf{W}$ . We want to model these data with a model  $m(\mathbf{P})$  depending on a set of parameters  $\mathbf{P}$ . For a parameter vector  $\mathbf{P}$ , the  $\chi^2$  is defined as:

$$\chi^2(\mathbf{P}) = (\mathbf{M}(\mathbf{P}) - \mathbf{D})^T \mathbf{W} (\mathbf{M}(\mathbf{P}) - \mathbf{D}) = \mathbf{R}^T(\mathbf{P}) \mathbf{W} \mathbf{R}(\mathbf{P}) \quad (\text{B.1})$$

where  $\mathbf{M}(\mathbf{P})$  is the vector of the model predicted values for the  $N$  data points. The vector  $\mathbf{R}(\mathbf{P})$  is the residuals vector.

In order to find the set of parameters  $\hat{\mathbf{P}}$  that minimizes the  $\chi^2$  function, we search for the zero of the  $\chi^2$  gradient

<sup>15</sup> <http://astrometry.net/>

that verifies  $\nabla_{\mathbf{P}} \chi^2(\hat{\mathbf{P}}) = 0$ . The algorithm used is the iterative multi-dimensional Gauss-Newton method, that we describe hereafter.

We start the minimisation with a first guessed value for the parameters  $\mathbf{P}_0$ . A Taylor expansion at first order of the  $\nabla_{\mathbf{P}} \chi^2$  function can be performed around the starting point  $\mathbf{P}_0$  and gives:

$$\nabla_{\mathbf{P}} \chi^2(\mathbf{P}_1) \stackrel{\mathbf{P} \approx \mathbf{P}_0}{\approx} 2\mathbf{J}_0^T \mathbf{W} \mathbf{R}_0 + 2\mathbf{J}_0^T \mathbf{W} \mathbf{J}_0 \delta \mathbf{P}_1 + \dots \quad (\text{B.2})$$

with  $\delta \mathbf{P}_1 = \mathbf{P}_1 - \mathbf{P}_0$  and  $\mathbf{J}_0 = \nabla_{\mathbf{P}} \mathbf{M}(\mathbf{P}_0)$  the Jacobian matrix of the model evaluated at  $\mathbf{P}_0$ . Note that for a linear model, i.e., a model that can be written as  $m(\mathbf{P}|\mathbf{Z}) = \sum_{i=1}^N P_i f(\mathbf{Z})$ , the  $\nabla_{\mathbf{P}} \chi^2(\mathbf{P})$  is exactly equal to its first order Taylor expansion.

The zero of the function is then approached solving the equation  $\nabla_{\mathbf{P}} \chi^2(\mathbf{P}_1) = \mathbf{0}$ :

$$\nabla_{\mathbf{P}} \chi^2(\mathbf{P}_1) = \mathbf{0} \Rightarrow \mathbf{P}_1 = \mathbf{P}_0 - \left( \mathbf{J}_0^T \mathbf{W} \mathbf{J}_0 \right)^{-1} \mathbf{J}_0^T \mathbf{W} \mathbf{R}_0. \quad (\text{B.3})$$

Because of the approximation coming from the Taylor expansion and of the finite numerical accuracy of the Jacobian matrix computation, it is unlikely that the  $\mathbf{P}_1$  found cancels exactly the  $\chi^2$  gradient.

We then search for the  $\alpha$  value that minimizes the  $\chi^2$  function along the line parametrised by the vector  $\alpha_1 \delta \mathbf{P}_1$  where  $\alpha_1$  is a real number. The  $\mathbf{P}_1$  value solution then writes:

$$\mathbf{P}_1 = \mathbf{P}_0 - \hat{\alpha}_1 \left( \mathbf{J}_0^T \mathbf{W} \mathbf{J}_0 \right)^{-1} \mathbf{J}_0^T \mathbf{W} \mathbf{R}_0. \quad (\text{B.4})$$

The process is iterated  $K$  times:

$$\mathbf{P}_{k+1} = \mathbf{P}_k - \hat{\alpha}_{k+1} \left( \mathbf{J}_k^T \mathbf{W} \mathbf{J}_k \right)^{-1} \mathbf{J}_k^T \mathbf{W} \mathbf{R}_k \quad (\text{B.5})$$

until a convergence criteria is reached. For example when the value of  $\chi^2(\mathbf{P}_k)$  or  $\mathbf{P}_k$  evolution with  $k$  gets below a certain threshold.

The best fitting model is then considered to be the one parametrised by the  $k$ th vector:  $\hat{\mathbf{P}} \approx \mathbf{P}_k$ . The covariance matrix of the  $\mathbf{P}_k$  parameters is obtained as the Hessian matrix at the minimum  $\chi^2$ :

$$\mathbf{C}(\hat{\mathbf{P}}) = \left( \mathbf{J}_k^T \mathbf{W} \mathbf{J}_k \right)^{-1}. \quad (\text{B.6})$$

In `Spectractor`, we also implemented the possibility to limit the  $\mathbf{P}$  search within given bounds (for instance we can impose that the amplitudes are all positive). We found that such bounds help the algorithm to converge.

## Appendix C: Second order penalisation

Regularisation techniques involving the total variation are often used in image analysis for de-noising or deconvolution while recovering sharp edges. One way to justify the use of a penalisation with the discretised Laplacian is to understand that it entails an automatic bound on the total variation. We show it in the following.

Recall some notations. The complete cost to minimize is :

$$\begin{aligned} \mathcal{E}(\mathbf{A}|\mathbf{r}_c, \mathbf{P}) &= (\mathbf{D} - \mathbf{M}\mathbf{A})^T \mathbf{W} (\mathbf{D} - \mathbf{M}\mathbf{A}) \\ &\quad + r(\mathbf{A} - \mathbf{A}_0)^T \mathbf{Q} (\mathbf{A} - \mathbf{A}_0) \\ &= \chi^2(\mathbf{A}|\mathbf{r}_c, \mathbf{P}) + r\chi_{\text{pen}}^2(\mathbf{A}|\mathbf{A}_0), \end{aligned} \quad (\text{C.1})$$

$$\mathbf{A}_0 = \mathbf{A}^{(1D)} \quad (\text{C.2})$$

$\mathbf{D}$  is the data vector,  $\mathbf{M}$  the design matrix and  $\mathbf{A}$  is the amplitude vector which gives the spectrogram and that we wish to obtain.  $\mathbf{W}$  is the inverse of the covariance matrix so that if we have all the true parameters for  $\mathbf{A}$ ,  $\mathbf{r}_c$  and  $\mathbf{P}$ , then  $\chi^2(\mathbf{A}|\mathbf{r}_c, \mathbf{P})$  is the sum of the squares of the residuals and thus is the realisation of a random variable following a  $\chi^2$  law with  $N_x N_y$  degrees of freedom, hence the name of the cost as  $\chi^2$ .

The penalisation term  $\chi_{\text{pen}}^2(\mathbf{A}|\mathbf{A}_0) = (\mathbf{A} - \mathbf{A}_0)^T \mathbf{Q} (\mathbf{A} - \mathbf{A}_0)$  is also a quadratic term and for  $\mathbf{Q} = \mathbf{L}^T \mathbf{U}^T \mathbf{U} \mathbf{L}$  with the Laplacian operator  $\mathbf{L} = -\mathbf{D}^T \mathbf{D}$ :

$$\mathbf{L} = \begin{pmatrix} -1 & 1 & 0 & 0 & \cdots & 0 & 0 \\ 1 & -2 & 1 & 0 & \cdots & 0 & 0 \\ 0 & 1 & -2 & 1 & \cdots & 0 & 0 \\ \vdots & \ddots & \ddots & \ddots & \ddots & \vdots & \vdots \\ 0 & 0 & 0 & 0 & \cdots & -2 & 1 \\ 0 & 0 & 0 & 0 & \cdots & 1 & -1 \end{pmatrix} \quad (\text{C.3})$$

$$\mathbf{D} = \begin{pmatrix} 1 & -1 & 0 & 0 & \cdots & 0 & 0 \\ 0 & 1 & -1 & 0 & \cdots & 0 & 0 \\ 0 & 0 & 1 & -1 & \cdots & 0 & 0 \\ \vdots & \ddots & \ddots & \ddots & \ddots & \vdots & \vdots \\ 0 & 0 & 0 & 0 & \cdots & 1 & -1 \\ 0 & 0 & 0 & 0 & \cdots & 0 & 1 \end{pmatrix} \quad (\text{C.4})$$

and  $\mathbf{U}$  is such that

$$\mathbf{U} = \begin{pmatrix} 1/\sigma_{A_{1D}^{(1)}} & 0 & \cdots & 0 \\ 0 & 1/\sigma_{A_{1D}^{(2)}} & \cdots & 0 \\ \vdots & \ddots & \ddots & \vdots \\ 0 & 0 & \cdots & 1/\sigma_{A_{1D}^{(N_x)}} \end{pmatrix} \quad (\text{C.5})$$

we get  $\chi_{\text{pen}}^2(\mathbf{A}|\mathbf{A}_0) = (\mathbf{U}\mathbf{L}(\mathbf{A} - \mathbf{A}_0))^T (\mathbf{U}\mathbf{L}(\mathbf{A} - \mathbf{A}_0))$  and is the quadratic norm (or the squared euclidean norm) of the vector  $\mathbf{U}\mathbf{L}(\mathbf{A} - \mathbf{A}_0)$  denoted  $\|\mathbf{U}\mathbf{L}(\mathbf{A} - \mathbf{A}_0)\|_2^2$ .

If we interpret  $\mathbf{A}$  as the discretisation of a continuous spectrogram  $a$  by setting  $A^{(i)} = a\left(\frac{i}{N_x}\right)$ , and  $\sigma$  is a function such that  $\sigma\left(\frac{i}{N_x}\right) = \sigma_{A_{1D}^{(i)}}$ , a continuous analogue of this term would be a term of the form

$$\|(a - a_0)''\|_{2,\sigma}^2 = \int_0^1 [(a - a_0)''(x)]^2 \frac{dx}{\sigma^2(x)}$$

where  $a, a_0$  would be functions whose  $\mathbf{A}, \mathbf{A}_0$  are discretisations. As a simple consequence, one has

$$\lim_{N_x \rightarrow \infty} N_x^3 \chi_{\text{pen}}^2(\mathbf{A}|\mathbf{A}_0) = \|(a - a_0)''\|_{2,\sigma}^2 \quad (\text{C.6})$$

since  $N_x \mathbf{D} \sim -\frac{d}{dx}$ .

The total variation distance is defined as the (weighted) norm-1 of the gradient operator, in functional term :

$$\|(a - a_0)'\|_{1,\sigma} = \int_0^1 |(a - a_0)'(x)| \frac{dx}{\sigma(x)}.$$

Note also that

$$\lim_{N_x \rightarrow \infty} \sum_{i=1}^{N_x} |\mathbf{U}\mathbf{D}(\mathbf{A} - \mathbf{A}_0)| = \|(a - a_0)'\|_{1,\sigma}. \quad (\text{C.7})$$

However by a simple argument, one can show that the 2-norm of the second derivative controls the 1-norm of the first derivative so that minimizing the former entails that we minimize also the latter. In order to prove it, let  $f(x) = a(x) - a_0(x)$ , we get

$$f'(x) = f'(0) + \int_0^x f''(s) ds = f'(0) + \int_0^x f''(s) \sigma(s) \frac{ds}{\sigma(s)} \quad (\text{C.8})$$

$$\leq f'(0) + \left( \int_0^x (f''(s))^2 \frac{ds}{\sigma(s)^2} \right)^{1/2} \left( \int_0^x \sigma^2(s) ds \right)^{1/2}. \quad (\text{C.9})$$

Thus, under the supplementary constraint that  $a'(0) = a_0'(0)$ , we have

$$\|(a - a_0)'\|_{1,\sigma} \leq \left( \int_0^1 \sigma^2(s) ds \right)^{1/2} \|(a - a_0)''\|_{2,\sigma}. \quad (\text{C.10})$$

The discrete analogue is, asymptotically in  $N_x \rightarrow +\infty$ :

$$\sum_{i=1}^{N_x} |\mathbf{U}\mathbf{D}(\mathbf{A} - \mathbf{A}_0)|_{1,\sigma} \leq N_x \sqrt{\text{Tr}(\mathbf{U}^{-2}) \chi_{\text{pen}}^2(\mathbf{A}|\mathbf{A}_0)}. \quad (\text{C.11})$$

This shows that regularisation using the weighted quadratic second order derivative ensures automatically an upper bound of the weighted total variation norm. So, while being computationally a lot faster, regularizing by the weighted quadratic norm of the second order derivative ensures an upper bound on the regularisation via the weighted total variation norm. Since the usual advantages of the weighted total variation norm (absence of assumption of a second order derivative or research of a sparse minimizer) are not important here, the choice of the weighted quadratic norm of the second order derivative as a loss function is completely pertinent.

## Appendix D: Atmospheric Differential Refraction

The Atmospheric Differential Refraction (ADR) depends mostly on the pressure, the temperature, the airmass and loosely on the atmosphere humidity.

In our wavelength calibration process for CALSPEC stars, the absorption line that weights most in the fit is the main dioxygen line at 762.1 nm. If the ADR is not correctly modelled and taken into account in the wavelength calibration, shifts of the absorption line minima towards the blue part of the spectrum can be observed through the night while the airmass of the star changes.

This is illustrated in the left panels of Figures D.1 and D.2. On the right panels, the ADR effect is included to the wavelength calibration process through a wavelength dependent shift of the order 0 centroid  $\delta u_0^{(\text{ADR})}(\lambda)$ . We observe that this procedure absorbs most of the line shifts when the dispersion axis is not orthogonal to the zenith direction.

For completeness, in Figure D.3 we represent the angle conventions used in **Spectractor** to compute correctly the zenith direction in the image.

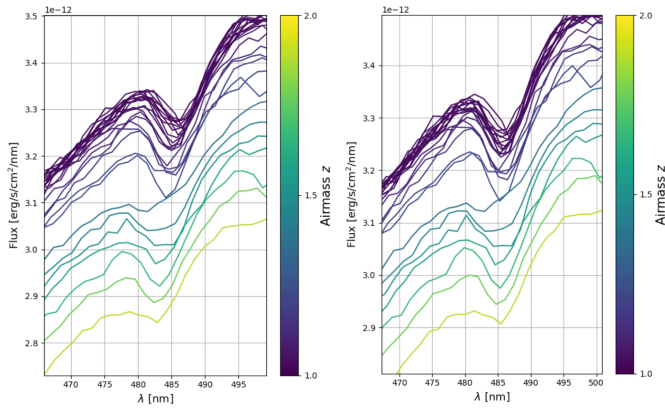


**Fig. D.1.** Absorption line  $H\beta$  at 486.3 nm of CALSPEC star HD111980 observed during the night of 2017, May 30th while it goes from an airmass of 1 to approximately 2. *Left:* without ADR effect being modelled in the wavelength calibration process. *Right:* with the ADR effect included in the wavelength calibration process. The profiles are better aligned.

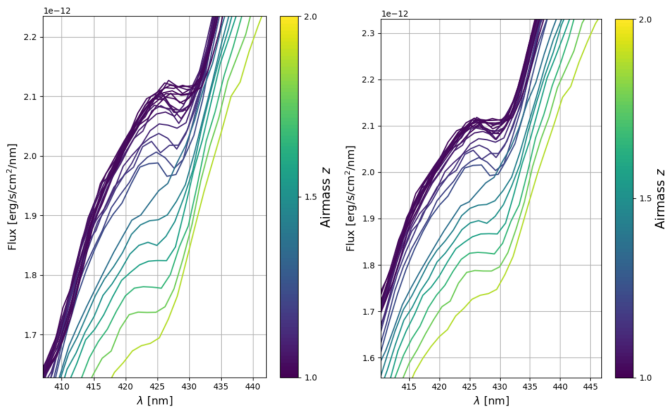


**Fig. D.2.** Same as Figure D.1 but for a  $Fe$  absorption line at 430.8 nm.

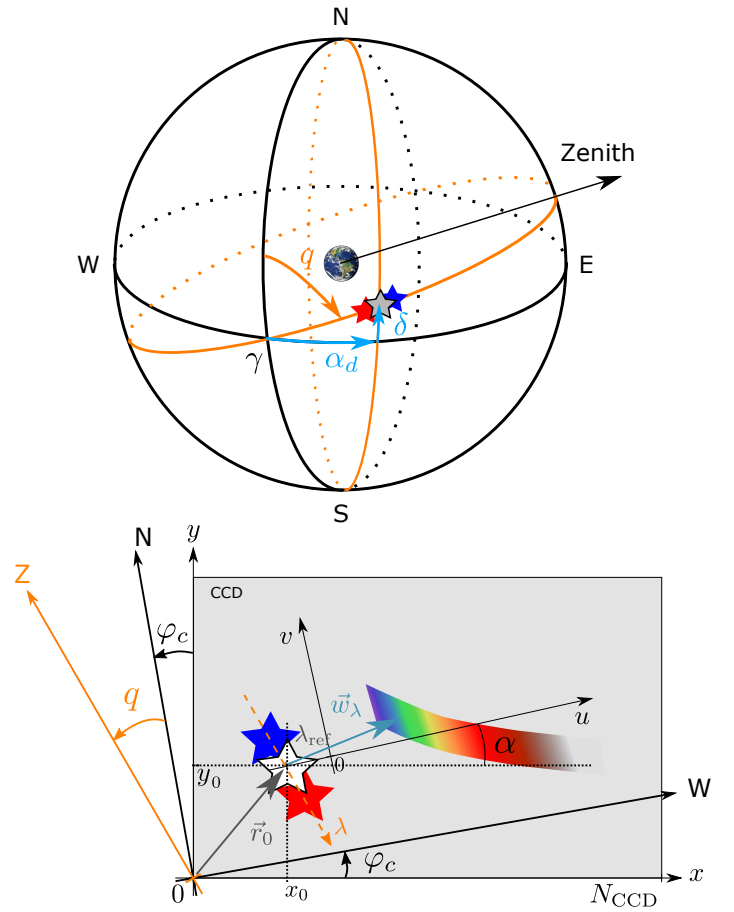


**Fig. D.3.** Angle conventions for the prediction of the ADR effect in the spectrogram. *Top:* celestial coordinates in the right ascension  $\alpha_d$  (RA) and declination  $\delta$  (DEC) system, with  $q$  the parallactic angle which sets the direction of the local zenith positively eastward. *Bottom:* angle conventions in the Spectractor image, with  $\varphi_c$  the North-West axis angle with respect to the camera horizontal axis.